CAN1-mediated autophagosome size regulation fine-tunes phosphate starvation tolerance in *Arabidopsis thaliana*

David Görg[1], Fiona Smith[1], Klara Machalett[1,2], Falko Koblenz[1], Ymy Thi Ngo[1], Sascha Höhne[1], Julian Arndt[1], Sylvestre Marillonnet[3], Nenad Grujic[4], Richard Imre[4,5], Karl Mechtler[4,5], Yasin Dagdas[6], and Christin Naumann[1*]

[1]Department of Molecular Signal Processing, Leibniz Institute of Plant Biochemistry, 06120 Halle (Saale), Germany

[2]Institute of Biochemistry and Biotechnology, Martin Luther University Halle-Wittenberg, Halle (Saale), Germany

[3]Department of Cell and Metabolic Biology, Leibniz Institute of Plant Biochemistry, 06120 Halle (Saale), Germany

[4]Gregor Mendel Institute of Molecular Plant Biology, Vienna, Austria

[5]Research Institute of Molecular Pathology (IMP), Vienna BioCenter (VBC), Vienna, Austria

[6]Heidelberg University, Centre for Organismal Studies, Heidelberg, Germany

*Corresponding author e-mail: cnaumann@ipb-halle.de

ORCID IDs: 0000-0002-9712-5728 (D.G.); 0009-0004-4740-3197 (K.M.); 0000-0002-4263-797X (S.M.); 0000-0002-9502-355X (Y.D.); 0000-0001-6972-155X (C.N.)

ABSTRACT

Inorganic phosphate (Pi) availability determines root development and plant performance. In *Arabidopsis thaliana*, external Pi is sensed by root tips and Pi limitation triggers ER stress–induced autophagy, yet the physiological impact and mechanisms controlling autophagosome biogenesis remain unclear. Here, we identify CAN1 (COMPONENT OF AUTOPHAGIC NETWORK) as a novel plant-specific regulator of autophagosome size in local Pi sensing. CAN1 associates with the plasma membrane-ER tethering protein VAP27-1 and binds to Pi-responsive ATG8 isoforms through conserved interaction motifs. Loss of CAN1 augments ER stress resistance by reducing autophagosome size in Pi-deprived root tips. Our findings establish CAN1 as a determinant of autophagosome size at the ER membrane. Thus, CAN1 functions as a molecular link between Pi-dependent ER stress signaling and fine-tuning of autophagic capacity.

32 **INTRODUCTION**

33 Plant growth and development are tightly constrained by nutrient availability in soil.
34 Phosphorus, primarily absorbed as inorganic phosphate (Pi), is the second most critical
35 macronutrient, and Pi availability is often limited by complex chemical interactions with
36 associated metals (e.g. Fe, Al) and their (Abel 2017; Abel and Naumann 2024; Lambers et al.
37 2015; Shen et al. 2011). To enhance Pi acquisition for maintaining cellular Pi homeostasis,
38 plants undergo extensive developmental and metabolic reprogramming, which includes
39 remodeling of root system architecture and chemical modification of the rhizosphere,
40 respectively (Crombez et al. 2019; Giehl and von Wiren 2014; Kellermeier et al. 2014; Yang
41 et al. 2024). In growing root tips of *Arabidopsis thaliana*, low external Pi rapidly reduces cell
42 elongation and progressively inhibits cell division (Balzergue et al. 2017; Clua et al. 2024;
43 Maniero et al. 2024; Muller et al. 2015; Naumann et al. 2022). The single ER-resident
44 P5A-type ATPase PHOSPHATE DEFICIENCY RESPONSE 2 (PDR2) and the apoplastic
45 ferroxidase LOW PHOSPHATE ROOT 1 (LPR1) form the core module of local Pi sensing in
46 root tips (Svistoonoff et al. 2007; Ticconi et al. 2001; Ticconi et al. 2009). Decreasing Pi-
47 availability activates LPR1 by facilitating access to its substrate (Fe^{2+}), triggering cell-type-
48 specific Fe^{3+} accumulation, formation of reactive oxygen species (ROS), and cell wall
49 modifications, which interrupts cellular communication and consequently root growth
50 (Balzergue et al. 2017; Gutierrez-Alanis et al. 2017; Muller et al. 2015; Naumann et al. 2022).
51 PDR2 counteracts LPR1 function by maintaining root tip Fe homeostasis through an unknown
52 mechanism (Jakobsen et al. 2005; Muller et al. 2015; Naumann et al. 2022; Naumann et al.
53 2019; Ticconi et al. 2009). Biochemical and structural studies reveal that P5A-type ATPases
54 (P5As) act as membrane-helix dislocases that assist transmembrane protein insertion and
55 remove mistargeted proteins, thereby safeguarding ER function and organelle integrity (Ji et
56 al. 2024; Li et al. 2024; McKenna et al. 2022; McKenna et al. 2020). Disruption of P5A
57 activity is detrimental across eukaryotes, affecting neuronal development in animals and

58 causing pleiotropic ER-associated defects in yeast (Feng et al. 2020; Li et al. 2021; Qin et al.
59 2020; Sim and Park 2023). In plants, PDR2 function in root tips is linked to Pi-dependent ER
60 stress-induced autophagy (Naumann et al. 2019; Stephani et al. 2020; Ticconi et al. 2009).
61 Autophagy is a conserved degradation pathway essential for protein and organelle quality
62 control, cellular homeostasis, and stress adaptation (Gross et al. 2025; Liu and Bassham 2012;
63 Petersen et al. 2024; Su et al. 2020). Damaged organelles or protein aggregates are
64 sequestered into double-membrane autophagosomes, typically 0.5–1.5 μm in diameter, which
65 subsequently fuse with the vacuole for cargo degradation (Nakatogawa 2020; Zhao et al.
66 2022; Zheng et al. 2018). Autophagosome biogenesis originates at ER-associated phagophore
67 initiation sites through PI3K complex (ATG6–VPS15–VPS34–ATG14) recruitment and
68 progresses via ATG8 lipidation, mediated by the ATG12–ATG5–ATG16 complex.
69 Additional regulators, such as SH3P2, interact with ATG8 and the PI3K complex to support
70 phagophore expansion, cargo loading, vacuolar targeting, and possibly autophagosome size
71 control (Nascimbeni et al. 2017; Walczak and Martens 2013; Zhuang et al. 2013). Selective
72 autophagy receptors, including NBR1 (Jung et al. 2020; Svenning et al. 2011) and C53
73 (Stephani et al. 2020), deliver defined cargos to the phagophore through ATG8 interaction
74 motifs (AIMs), and cargo characteristics can directly influence autophagosome dimension
75 (Johansen and Lamark 2020). ATG8 isoforms enable organ- and stress-specific autophagy
76 responses as illustrated by the differential complementation of carbon and nitrogen starvation
77 phenotypes (Del Chiaro et al. 2025; Dong et al. 2025; Liu et al. 2021; Thompson et al. 2005).
78 Beyond nutrient starvation, local Pi sensing in root tips and Pi deficiency in green tissues
79 triggers iron-mediated ER stress-induced autophagy, likely originating from cargo overload
80 within the secretory pathway (Naumann et al. 2019; Yoshitake et al. 2022). Notably,
81 autophagosome size is highly variable and strongly shaped by the nature of the target, yet how
82 autophagosome dimensions are controlled during biogenesis remains unknown. Emerging
83 evidence suggests that ER-associated proteins at phagophore initiation sites are likely central

84 to autophagosome size determination; however, the molecular mechanism and components
85 involved remain elusive.
86
87 Here, using quantitative proteomics and interaction assays in Arabidopsis, we report a novel
88 COMPONENT OF THE AUTOPHAGIC NETWORK (CAN1) as a plant-specific regulator
89 of autophagosome size during Pi limitation. CAN1 associates with the ER–plasma membrane
90 tethering protein VAP27-1 and the ER-membrane embedded glycosylation complex
91 component DGL1, interacts with root tip-localized ATG8B and ATG8C isoforms via
92 conserved AIM motifs, and its loss of function results in smaller autophagosomes and
93 enhanced ER stress resistance. Through its role in Pi-mediated autophagy, CAN1 shapes
94 autophagosome biogenesis, establishing an ER-associated regulatory network that converges
95 with ATG8-mediated, organ-specific autophagy.
96
97 **RESULTS**
98 **Phosphate limitation induces ATG8 isoform specific ER stress mediated autophagy**
99 Tissue specific expression of ATG8 isoforms (ATG8A-ATG8I) in *Arabidopsis thaliana*
100 mediate the autophagic response under distinct stress conditions (Del Chiaro et al. 2025;
101 Dong et al. 2025). To investigate their roles in local root Pi sensing, we monitored native
102 promoter-driven GFP-ATG8 protein fusions (*pATG8x::GFP-ATG8x*) (Del Chiaro et al. 2025)
103 for autophagosome formation in wildtype (WT) seedlings transferred from Pi-replete (+Pi) to
104 Pi-deprived (-Pi) conditions as well as after exposure to carbon starvation (-C) and
105 tunicamycin-induced (+TM) ER stress (Fig. S1). Consistent with previous reports, GFP
106 fluorescence was largely absent in basal (+Pi) condition for most ATG8 isoforms with the
107 exception of ATG8A and ATG8F (Del Chiaro et al. 2025; Dong et al. 2025; Thompson et al.
108 2005). Upon carbon starvation, all tested lines exhibited GFP-positive puncta formation in the
109 root transition zone and, to a lower extent, in the root tip, indicative of bulk autophagy

110 activation independent of isoform specificity (Fig. S1). Likewise, TM treatment induced
111 autophagosome formation in the transition zone of all transgenic GFP-ATG8 lines. Notably,
112 Pi deprivation selectively activated autophagosome formation in root tips expressing GFP-
113 ATG8 fusion isoforms B, C, and E suggesting an ATG8 isoform-specific involvement in Pi
114 sensing (Fig. 1a, Fig. S1). Given that local root Pi sensing triggers ER stress-mediated
115 autophagy in Pi limitation via the PDR2–LPR1 module (Naumann et al. 2019; Stephani et al.
116 2020), we introgressed *pATG8B/C::GFP-ATG8B/C* transgenes into the Pi-sensitive
117 *pdr2* mutant and monitored autophagosome formation following Pi deprivation. When
118 compared to +Pi conditions, the number of GFP-ATG8B labelled autophagosomes increased
119 2-fold and 2.5-fold in wildtype and *pdr2* roots, respectively, with no significant changes in
120 *ATG8* transcript levels (Fig. 1, Fig. S2a). Interestingly, the number of GFP-ATG8C labelled
121 puncta increased significantly only in *pdr2,* suggesting a specific role in ER quality control,
122 which is supported by enhanced autophagosome formation upon TM treatment (Fig. 1).
123 To assess ATG8 isoform-specific functionality, we examined local Pi sensing in the ATG8-
124 deficient nonuple mutant *Δatg8* (Del Chiaro et al. 2025), alongside complementation lines
125 expressing GFP-ATG8A or GFP-ATG8H, representing the two major ATG8 clades in
126 *Arabidopsis* (Rogov et al. 2023). *Δatg8* mutants exhibited modest root growth defects in Pi
127 deprivation, indicative of enhanced ER stress sensitivity (Fig. S2b). Notably, ectopic
128 expression of either ATG8A or ATG8H did not rescue this phenotype, implying that
129 autophagosome induction in local Pi sensing may involve isoform-specific functions.

130 **Local Pi sensing remodels autophagy-dependent root tip proteome**

131 To elucidate the biological role of ER stress-induced autophagy in local Pi sensing and
132 uncover novel components, we employed two complementary mass spectrometry-based
133 screening approaches. Our working hypothesis posits that proteins regulated in an autophagy-
134 dependent mode during Pi sensing should (i) exhibit altered abundances in autophagy-
135 deficient mutants such as *atg2*, and (ii) physically interact with ATG8 isoforms. First, we

136 performed proteomic profiling of wildtype, *pdr2*, and *atg2* root tips using tandem mass tag-
137 based quantitative mass spectrometry (TMT-MS). Seedlings were germinated in Pi-
138 sufficiency and subsequently transferred to control (+Pi) or ER stress-inducing (−Pi or +TM)
139 conditions. Comparative analysis revealed that either ER stress condition caused pronounced
140 proteomic shifts in root tips, with *atg2* displaying a significantly higher number of
141 differentially abundant proteins relative to wildtype and *pdr2* (Fig. 2a, Fig. S3a, Data S1). We
142 next analyzed the protein abundances in ER stress conditions in *atg2* in comparison to WT or
143 *pdr2*. For Pi-deprivation 89 proteins were increased in *atg2* but not in wildtype or *pdr2* root
144 tips, suggesting autophagy-dependent regulation (Fig.2b, Fig. S3b). This set includes core
145 autophagy components such as ATG4, multiple ATG8 isoforms, and selective autophagy
146 receptors, NBR1 and C53, previously implicated in ER stress responses and Pi signaling
147 (Picchianti et al. 2023; Stephani et al. 2021; Stephani et al. 2020; Wild et al. 2014).
148 Enrichment of these proteins reinforced the validity of our experimental design and highlights
149 a functional role of autophagy in maintaining proteostasis during local Pi perception.
150 Second, to identify Pi-responsive ATG8 interactors, we performed immunoprecipitation
151 coupled with mass spectrometry (IP-MS) using wildtype and *pdr2* lines expressing
152 *p35S::GFP-ATG8A* (Fig. S3d, e; Data S2). This screen revealed over 300 potential
153 interactors, including ATG8B and ATG8C as well as NBR1 and C53, which are established
154 ATG8 interactors (Stephani et al. 2020; Wilfling et al. 2020; Zhao et al. 2022).
155 To discover functionally relevant ATG8-associated proteins in Pi-deprivation, we cross-
156 referenced the ATG8A interactome (Fig. 2c,d) with the set of 89 proteins stabilized in *atg2*
157 (Fig. 2b), which revealed ATG8B, ATG8C, NBR1 and an uncharacterized protein
158 (AT5G40690), among the most enriched candidates across both datasets (Fig. 2e). Consistent
159 detection of AT5G40690, suggests a novel function in autophagy-dependent Pi sensing and
160 root proteostasis. We therefore refer to AT5G40690 as CAN1 (COMPONENT OF
161 AUTOPHAGIC NETWORK).

162 **CAN1 is evolutionally conserved among land plant species**

163 While the core autophagy machinery is conserved across plants, the identification of
164 modulators fine-tuning the autophagic pathway remains an active area of investigation
165 (Cadena-Ramos and De-la-Pena 2024; Gross et al. 2025; Stephani and Dagdas 2020).
166 AT5G40690 encodes a small, 210-amino-acid protein, expressed from a single exon.
167 Phylogenetic analysis revealed that CAN1 is exclusive to and conserved across mostly all
168 major land plant lineages apart from ferns and gymnosperms (Fig. 3a, Fig. S4).
169 Notably, in a subset of angiosperms, including both monocot and dicot species but not
170 bryophytes and *Amborella trichopoda*, we identified additional gene homologs encoding
171 truncated proteins (~110 amino acid residues), that lack the C-terminal domain present in
172 canonical CAN1 orthologs (Fig. 3a, Fig. S4). In Arabidopsis, two such paralogs, HRG1
173 (AT2G411730) and HRG2 (AT5G24640) have been implicated in reactive oxygen species
174 (ROS)-mediated root meristem maintenance (Gong et al. 2021). These findings suggest
175 functional divergence or neofunctionalization of HRG proteins within specific angiosperm
176 lineages such as the Brassicaceae.
177 Expression analysis in whole seedlings revealed consistent upregulation of *CAN1* transcript
178 levels in autophagy-deficient mutants (*atg2*, *atg5*, *atg7*, and *atg9*) compared to the wildtype
179 control (Fig. 3b). To investigate organ- and tissue-specific *CAN1* expression, we generated
180 transgenic *pCAN1::GUS* wildtype and *atg5* mutant lines (Fig. 3b-d). In wildtype, *CAN1*
181 promoter activity was predominantly detected in root tissues, including lateral roots and root
182 hairs, with increased activity in the root-shoot junction, while only weak GUS reporter signals
183 were observed in the tip region of cotyledons and true leaves as well as in flowers and
184 developing siliques (Fig. 3b,c). Interestingly, in the *atg5* background, the spatial distribution
185 of *CAN1* promoter activity was comparable to wildtype, but markedly enhanced as evidenced
186 by intense GUS staining, which correlates to elevated *CAN1* transcript levels measured in
187 autophagy-deficient lines (Fig. 3b, d). Collectively, the evolutionary conservation of *CAN1*,

188 its dominant expression in roots, and its transcriptional activation in autophagy mutants
189 support a role for *CAN1* in nutrient-dependent ER stress responses in land plants.

190 **CAN1 interacts with ATG8 in an AIM-dependent manner**

191 Co-immunoprecipitation of endogenous ATG8 with CAN1-mCherry expressed in
192 Arabidopsis roots experiencing ER stress (Fig. 4a) validated our initial IP-MS identification
193 of CAN1 as an ATG8 interactor (Fig. 2). We combined structural modeling with *in vitro* and
194 *in vivo* studies to determine the ATG8-binding site of CAN1. AlphaFold2 modelling indicated
195 CAN1 to be intrinsically disordered and predicted the presence of five putative ATG8-
196 interacting motif (AIM) consensus sequences (W/F/V-X-X-L/I/V), with AIM5 (aa 202-205)
197 being the best candidate followed by AIM4 (aa 183-189) (Fig. 4b; Fig. S5). Yeast two-hybrid
198 interaction assays indicated AIM5-dependent CAN1 binding to all ATG8 isoforms, and
199 strong interaction with ATG8G, H, and I (Fig. 4c). Transient expression of GFP fusions of
200 CAN1 in tobacco (*Nicotiana benthamiana*) and live cell imaging showed predominantly
201 cytosolic localization with partial net-like association reminiscent of ER structures (Fig. 4d).
202 Importantly, the subcellular localization observed for GFP-CAN1 was not altered by
203 introducing AIM4 and/or AIM5 deletions (Fig. 4e). Subsequent co-immunoprecipitation
204 analysis demonstrated the dominant role of AIM5 in CAN1 for ATG8 binding. While GFP-
205 CAN1 interacted with all RFP-ATG8 isoforms in tobacco leave extracts, which was also true
206 for GFP-CAN1$^{\Delta AIM4}$, deletion of AIM5 (GFP-CAN1$^{\Delta AIM5}$) abrogated CAN1 interaction with
207 most ATG8 isoforms except for ATG8E and ATG8G. As expected, deletion of AIM4 and
208 AIM5 abolished CAN1$^{\Delta AIM4/5}$ binding to any ATG8 isoform (Fig. 4f; Fig. S6). Collectively,
209 our results demonstrate differential interaction of CAN1 with ATG8 isoforms, which is
210 primarily mediated by AIM5.

211 **CAN1 functions in ER stress-dependent autophagy during local Pi sensing**

212 To investigate the relevance of CAN1–ATG8 interaction *in vivo* and its role for root
213 responses to ER stress, we monitored autophagosome formation in transgenic lines expressing

214 GFP-tagged CAN1 (*pCAN1::CAN1-GFP; pUBQ10::GFP-CAN1*) (Fig. 5a-d, Fig. S7).
215 Consistent with transient expression in tobacco (Fig. 4d, e), CAN1-GFP exhibited a diffuse
216 cytoplasmic distribution under control conditions, occasionally forming low-intensity puncta,
217 which remained unchanged when expressed in the low Pi-sensitive *pdr2* mutant (Fig. 5a, Fig.
218 S7a ,c).
219 Induction of ER stress by low Pi or TM treatment caused a rapid and robust increase in
220 CAN1-GFP puncta and partial net-like localization with further enhancement in *pdr2* root
221 cells (Fig. 5a,b). Importantly, CAN1 transcript levels and spatial expression in root tips
222 remained unaffected in all lines tested (Fig. S7e,f). CAN1-GFP puncta co-localized with
223 mCherry-ATG8E, demonstrating CAN1 association with autophagosomes (Fig. 5c,d, Fig. S7;
224 (Feng et al. 2022)). Consistently, no CAN1-GFP puncta were detected in the autophagy-
225 deficient *atg5* mutant although basal CAN1-GFP protein abundance was increased in *atg2*
226 and *atg5* (Fig. S8d). These findings demonstrate that CAN1 associates with the ER and
227 autophagosomes during ER stress in root tips, with a more pronounced response under Pi
228 limitation compared to pharmacological ER stress induction by TM (Fig. 5a–d).
229 To investigate CAN1 function in *Arabidopsis*, we first analyzed T-DNA insertion (3'UTR)
230 line (*SALK_092190*), which does not affect transcript abundance (Fig. S8a, b). We then
231 generated two independent loss-of-function alleles using CRISPR–Cas9-mediated genome
232 editing (Stuttmann et al. 2021): *can1-c1*, carrying an insertion resulting in a frameshift and
233 premature stop codon, and *can1-c3*, harboring a deletion predicted to have a similar effect
234 (Fig. S8b-c). Both mutant lines were phenotypically indistinguishable from wildtype during
235 germination and early root development (Fig. 5e, f). Under ER stress conditions, however,
236 both *can1* loss-of-function alleles exhibited increased survival on TM-containing medium,
237 indicating enhanced resistance (Fig. 5e). By contrast, no phenotypic differences were
238 observed under carbon or nitrogen starvation, a condition commonly used to activate bulk
239 autophagy (Fig. S8f-h).

240 We next examined the role of CAN1 in local Pi sensing. While both *can1* mutants were
241 significantly less sensitive to Pi deprivation, exhibiting enhanced primary root elongation,
242 *CAN1* overexpression (*pUBQ10::GFP-CAN1*) displayed the opposite root growth phenotype
243 on low Pi medium (Fig. 5f). However, the *CAN1* loss- and gain-of-function lines tested
244 were indistinguishable with respect to iron and callose accumulation in root tips, two
245 histochemical markers of local Pi sensing (Naumann et al. 2022) (Fig. S9).
246 Thus, our observations suggest that CAN1 is dispensable for bulk autophagy but functions in
247 ER stress-induced autophagy modulating root growth response under local Pi limitation.
248 **CAN1 facilitates autophagosome biogenesis through ER tethering with VAP27-1**
249 To elucidate a role of CAN1 in autophagy, we analysed the CAN1 interactome under basal
250 and ER stress conditions. Under ER stress, CAN1 associates with ATG8C and factors
251 involved in autophagosome maturation (ATG3, FREE1, SH3P2, VPS34, NBR1) and the ER
252 membrane (VAP27-1, DGL1), implicating CAN1 function in phagophore expansion (Fig. 6a;
253 Fig. S10a). Co-immunoprecipitation confirmed CAN1 interaction with NBR1 in wildtype and
254 *atg5* roots, restricted to ER stress in wildtype and stabilized by ConA treatment (Fig. 6b).
255 Considering the CAN1 localization and interactome under stress (Fig. 5c, Fig. 6a, Fig. S10a),
256 we tested interactions of CAN1 with DGL1, an ER quality control component of the OST
257 complex (Lerouxel et al. 2005), and with VAP27-1, an ER–PM tether involved in endocytosis
258 and mitophagy (Li et al. 2022; Man et al. 2024; Stefano et al. 2018; Wang et al. 2019). CAN1
259 co-immunoprecipitated with DGL1 (Fig. S10b), supporting ER recruitment of CAN1.
260 VAP27-1 also interacted with CAN1 in tobacco leaves and Arabidopsis roots under Pi
261 limitation or TM-induced ER stress (Fig. 6c,d), suggesting that CAN1 may anchor
262 phagophores to the ER via VAP27-1 interaction and, enable autophagosome membrane
263 expansion. Notably, GFP-ATG8A puncta were smaller in *can1-c1* root tips under Pi
264 limitation, while NBR1 turnover and autophagosome amount remained unaffected (Fig. 6e,f,

265 Fig. S10d, e), consistent with impaired phagophore expansion. CAN1 protein abundance
266 remained unchanged in ER stress (Fig. S8e, S10c).

267 **DISCUSSION**

268 Autophagy is essential for plant stress adaptation by maintaining cellular homeostasis under
269 fluctuating environmental conditions, yet the mechanisms determining autophagosome
270 maturation and size are largely unknown (Gross et al. 2025; Nakatogawa 2020; Zhao et al.
271 2022). In Arabidopsis, sensing of Pi limitation provokes iron-dependent ER stress response
272 followed by selective autophagy induction in growing root tips and photosynthetic tissues;
273 however the molecular determinants involved remain to be elucidated (Naumann et al. 2019;
274 Yoshitake et al. 2021; Yoshitake et al. 2022). Here we identify CAN1 as a novel
275 plant-specific regulator of autophagosome size during local root tip Pi-sensing. CAN1
276 associates with the ER through interaction with VAP27-1 and the OST complex subunit
277 DGL1, which is essential for ER protein quality control (Lerouxel et al. 2005) (Fig. 6).
278 Following ER stress perception, CAN1 associates with Pi-responsive ATG8 isoforms (B and
279 C) preferentially via its C-terminal AIM motif (Fig. 1, 4). Loss of CAN1 leads to significant
280 smaller autophagosomes and enhanced ER stress resistance (Fig. 5, 6) positioning CAN1
281 function in Pi-dependent ER stress signaling to the regulation of autophagosome biogenesis
282 and maturation.

283 Phagophore expansion occurs at ER-associated initiation sites where lipid flux, membrane
284 moulding, and cargo capture are coordinated (Gross et al. 2025; Liu et al. 2020; Liu and
285 Bassham 2012; Nascimbeni et al. 2017; Su et al. 2020; Zhuang et al. 2013). The ER–PM
286 tethering protein VAP27-1 is a key organizer of ER contact sites and supports mitophagy by
287 promoting ER-mitochondria connections necessary for phagophore expansion around
288 dysfunctional mitochondria (Li et al. 2022; Wang et al. 2019). VAP27-1 and its yeast
289 homologues further support ER-stress adaptation through interactions with soluble ER-phagy
290 receptors (Nthiga et al. 2020; Zhao et al. 2020). Although loss of VAP27-1 or DGL1 severely

291 compromises plant development due to their essential roles in membrane tethering and
292 N-glycosylation (Lerouxel et al. 2005; Wang et al. 2016), loss of CAN1 results instead in
293 enhanced ER stress resistance, indicating a more specialized function. The interaction of
294 CAN1 with VAP27-1 and DGL1 (Fig. 6) suggests that CAN1 contributes to stabilizing
295 phagophore–ER contacts, a process central to the controlled expansion of the autophagosome
296 membrane. We propose CAN1 modulates phagophore elongation by reinforcing ER–
297 membrane interfaces via VAP27-1 and acts together with Pi-responsive ATG8B/C isoforms
298 to establish a root cell-specific expansion regime for controlling autophagosome size. Such a
299 CAN1–VAP27-1–ATG8B/C complex may further provide the spatial framework necessary
300 for PI3K complex recruitment, thereby coordinating phagophore growth with cargo
301 encapsulation.
302 In the physiological context of growing root tips, the degradation of stress-induced cargo must
303 be balanced with the preservation of resources, especially under limited Pi availability. The
304 smaller autophagosomes observed in *can1* likely favour rapid turnover of small or diffusible
305 cargos during early ER stress perception via the LPR1-PDR2 module, conferring enhanced
306 resistance to low-Pi stress. Conversely, CAN1-dependent enlargement of autophagosomes in
307 wildtype may facilitate more efficient sequestration of larger, bulky cargo, albeit at reduced
308 throughput. This size-throughput trade-off aligns with the gradual response of Pi–Fe-linked
309 ER stress induction, where rapid turnover may facilitate cell adaptation and sustain plant
310 survival (Naumann et al. 2022; Naumann et al. 2019). CAN1 probably functions separate of
311 established regulators of autophagosome maturation and fusion, such as SH3P2 and FREE1,
312 whose loss is lethal, as well as autophagy inhibitors including COST1 and Rubicon-related
313 factors (Bao et al., 2020; Gao et al., 2015; Matsunaga et al., 2009; Walczak & Martens, 2013;
314 Zhuang et al., 2013). This reveals CAN1 function at a previously unrecognized regulatory
315 layer dedicated specifically to autophagosome size determination.

316 We propose that in roots CAN1 relocates to ER contact sites upon low Pi stress, engaging
317 ATG8B/C and VAP27-1 to stabilize PI3P complexes and regulate phagophore elongation.
318 Following autophagosome closure, NBR1 may recruit CAN1 for turnover, positioning CAN1
319 as a new local regulator of autophagosome expansion (Fig. 6g). Our findings unravelled a
320 complex regulatory network opening new avenues to dissect cargo selectivity and stress-
321 responsive remodelling of endomembrane systems for plant environmental adaptation.
322
323

324 **METHODS**

325 **Plant Materials**

326 All *Arabidopsis thaliana* lines used in this study originate from accession Columbia (Col-0).
327 Mutant lines *pdr2-1 (Ticconi et al. 2009)*, *lpr1 lpr2* (Svistoonoff et al. 2007), *ire1a ire 1b*
328 (Naumann et al. 2019), *atg5-4 (Suzuki et al. 2005)*, *atg2-1* (Wang et al. 2011), *atg7-3* (Lai et
329 al. 2011), *atg9-4* (Shin et al. 2014), *Δatg8 (Del Chiaro et al. 2025)* and transgenic lines
330 *p35S::GFP-ATG8A* (Thompson et al. 2005), *pdr2-1 x p35S::GFP-ATG8A* (Naumann et al.
331 2019), *35Spro::SpER-GFP-HDEL, pdr2-1 x 35Spro::SpER-GFP-HDEL (Ticconi et al.*
332 *2009), pUBQ10::mCherry-ATG8E, atg5-1 x pUBQ10::mCherry-ATG8E* (Stephani et al.
333 2020), *Δatg8* x *pUBQ10::ATG8A*, *Δatg8* x *pUBQ10::ATG8H* (Del Chiaro et al. 2025) were
334 previously described. T-DNA insertion line SALK_092190 was obtained from the European
335 Arabidopsis Stock Center (NASC). The *can1-c1* and *can1-c3* knockout lines were produced
336 by CRISPR-Cas9 technology (Stuttmann et al. 2021). Guide RNAs for target sequences
337 (AAGCGTGAAGGCAAACAACAC and AACCCGGAAAGCTTCAAACC) were designed
338 with CHOPCHOP (Labun et al. 2019) and cloned into pDGE332_M1 and pDGE334_M2E
339 constructs (Ordon et al. 2017; Stuttmann et al. 2021) and assembled in pDGE347 for
340 transformation. Double mutants were generated by genetic crossing and genotyped by PCR.
341 Primers used for cloning and genotyping are listed in Supplementary table 1 and all vectors
342 are listed in Supplementary table 2.

343 **Molecular Cloning**

344 The *AtDGL1* coding sequence (CDS) was synthesized by Thermo Fisher Scientific with three
345 point mutations introduced to eliminate internal BpiI recognition sites. The CDS was flanked
346 by BpiI sites to enable Golden Gate cloning and subcloned into the MoClo vector
347 pAGM1287, generating the level 0 *AtDGL1* module pNAU7. The *Arabidopsis thaliana*
348 Ubiquitin 10 (Ubi10) promoter was amplified by PCR from plasmid pRedRoot (Limpens et
349 al. 2004) and cloned as MoClo level 0 promoter modules pAGM11323, flanked by BpiI sites

350 GGAG and AATG for use as a standard promoter module, and pAGM11335, flanked by BpiI
351 sites GGAG and CCAT for assembly of transcriptional units containing N-terminal fusions.
352 An internal BpiI site within the promoter sequence was removed during cloning by
353 introducing a nucleotide substitution via the PCR primers. For N-terminal GFP fusion
354 constructs, modules pAGM11335 (pUbi10), pICSL30006 (N-terminal GFP tag, (Engler et al.
355 2014) pNAU7 (*AtDGL1*), and pAGM16841 (tNOS, (Gantner et al. 2018) were assembled in a
356 single BsaI Golden Gate reaction into pICH47742 (Weber et al. 2011), yielding
357 pUbi10::GFP-AtDGL1::tNOS.
358 For C-terminal GFP fusion constructs, modules pAGM11323 (pUbi10), pICSL50004 (C-
359 terminal GFP tag, (Engler et al. 2014) pNAU7 (*AtDGL1*), and pICH41421 (tNOS,) (Engler et
360 al. 2014) were assembled in a single BsaI Golden Gate reaction into pICH47742, yielding
361 pUbi10::AtDGL1-GFP::tNOS.
362 All other constructs were cloned via Gateway Technology.
363
364 **Plant Growth and Chemical Treatments**
365 Seeds were surface-sterilized and germinated on 1% (w/v) Phyto-Agar (Duchefa) containing
366 2.5 mM KH_2PO_4, pH 5.6 (high Pi or +Pi medium) or no Pi supplement (low Pi or –Pi
367 medium) as reported (Naumann et al. 2022). Agar media deficient in other nutrients (C, N, or
368 Fe) or supplemented with ER stress-agents were prepared as described (Naumann et al. 2022;
369 Naumann et al. 2019). The agar was routinely purified by repeated washing in deionized
370 water and subsequent dialysis using DOWEX G-55 anion exchanger (Ticconi et al. 2009).
371 For carbon starvation experiments on soil, 6 weeks-old plants grown under short-day
372 photoperiod were transferred to darkness for 6 days followed by 7 days of recovery in short-
373 day condition (Naumann et al. 2019; Qi et al. 2023; Thompson et al. 2005). Nutrient
374 limitation in aseptic conditions was performed as follows: For carbon starvation, seedlings
375 were transferred to carbon (sucrose) deficient media 5 days after germination and kept in the

376 dark for 12 days followed by 7 days of recovery on +Pi media. For nitrogen starvation, 5
377 days-old seedlings (after germination on +Pi) were transferred to nitrogen deficient media for
378 7 days.

379 **Chemical Treatments**

380 Tunicamycin (TM) and torin treatment were performed by transferring 5-day-old seedlings
381 (germinated on +Pi) to liquid media supplemented with 5 µg/mL TM, 1 µM torin or DMSO
382 (solvent) for 5-7 h. Concanamycin A (ConA) treatment was added to a final concentration of
383 1µM for the indicated time points (3-5 h).

384 **Histochemical staining**

385 GUS (β-glucuronidase) staining was conducted as described (Naumann et al. 2022).
386 Seedlings were incubated in GUS-staining solution (50 mM Na-phosphate, pH7.2; 0.5 mM
387 $K_3Fe(CN)_6$; 0.5 mM $K_4Fe(CN)_6$; 2mM X-Gluc; 10mM EDTA; 0,1% TritonX) at 37°C and
388 subsequently cleared using chloral hydrate solution (8:2:1 chloral hydrate:glycerol: ddH_2O).
389 Iron detection, based on Perls staining coupled to diaminobenzidine (DAB) intensification
390 (Perls/DAB staining) was performed as previously described (Muller et al. 2015) with minor
391 changes to the protocol. Plants were incubated for 10 min in 2% (v/v) HCl, 4% (w/v) K-
392 ferrocyanide (Perls staining), or K-ferricyanide (Turnbull staining). For DAB intensification,
393 plants were washed twice (ddH_2O) and incubated (15 min) in methanol containing 10 mM
394 Na-azide and 0.3% (v/v) H_2O_2. After washing with 100 mM Na-phosphate buffer (pH 7.4),
395 plants were incubated for 3 min in the same buffer containing 0.025% (w/v) DAB (Sigma-
396 Aldrich) and 0.005% (v/v) H_2O_2. The reaction was stopped by washing with 100 mM Na-
397 phosphate buffer (pH 7.4) and optically clearing with chloral hydrate, 1 g/ml 15% (v/v)
398 glycerol.

399 **Confocal Microscopy**

400 Samples were analyzed using a multizoom stereomicroscope (Nikon AZ100) for overview
401 images and a Zeiss AxioImager bright field microscope for detail images. Confocal

402 microscopy was done on a Zeiss LSM900. Imaging was performed with a ×20 air, ×40 water
403 or x63 water immersion objective using sequential acquisition. For each experiment, 7-10
404 individual samples were observed in three independent approaches. Images were processed
405 using ImageJ (Schindelin et al. 2012) software. Total puncta numbers were counted using the
406 MTB Cell Counter (Franke et al. 2015). Colocalization and Pearsons coefficient were
407 calculated using the BIOP FiJi Plugin.
408 Callose was stained for 1 h with 0.1% (w/v) aniline blue (AppliChem) in 100 mM Na-
409 phosphate buffer (pH 7.2) and carefully washed twice. Fluorescence was visualized using a
410 Zeiss LSM 900 confocal laser-scanning microscope (excitation 405 nm, emission 498 nm) in
411 100 mM Na-phosphate buffer (pH 7.2) (Muller et al. 2015).

412 **Autophagosome size determination**

413 Five-day old seedlings expressing *35S::GFP-ATG8A* in WT or *can1-c1* were transferred to
414 +Pi or -Pi for one day followed by liquid treatments to induce ER-stress by TM (5 µg/ml) or
415 torin (1 µM) treatments for 6 h. Primary root transition zones were imaged and Arivis Vision
416 4D 3.6.2 (arivis AG) was used for analysis. A custom pipeline to measure autophagosome
417 volume was set up using the Blob Finder with the following parameters: average size 2 µm,
418 probability threshold 55%, split sensitivity 50%. Sphericity was set to > 0.65 and a segment
419 feature filter was applied to ≥ 0.6 μm^2.

420 **Transient expression in *N. benthamiana***

421 Leaves of 6-week-old tobacco (*Nicotiana benthamiana*) plants were co-infiltrated with *A.*
422 *tumefaciens* harboring the respective plasmid. After 3 d, leaf discs were analyzed by confocal
423 laser scanning microscopy (GFP: excitation 488 nm, emission 493-537 nm; mCherry:
424 excitation 555 nm, emission 582-631 nm; chlorophyll autofluorescence: excitation 633 nm,
425 emission, 669-722 nm).

426 **Yeast-two-hybrid assay**

427 To perform direct Y2H test, the full length CAN1 as well as $CAN1^{F183A, V186A,}$ $CAN1^{W202A,}$

428 ^{V205A} and CAN1$^{F183A, V186A, W202A, V205A}$ (CAN1$^{\Delta AIM4}$, CAN1$^{\Delta AIM5}$ and CAN1$^{\Delta AIM4,5}$
429 respectively), were cloned into the pDEST32 (Invitrogen) vector using gateway technology,
430 to create protein fusions with the Gal4 DNA binding domain. All nine Arabidopsis ATG8
431 isoforms were cloned into the prey pDEST22 vector to obtain Gal4 activation fusions.
432 The bait and prey vectors to be tested for interaction of the fusion proteins were co-
433 transformed into *S. cerevisiae* strain PJ69-4a using the standard LiOAc method (Gietz and
434 Schiestl 2007). The yeast was spotted on plates with vector selective media DDO (double
435 drop out media: SD/-Leu/-Trp) and were grown for 4-5 days at 30°C. Two independent
436 colonies of each transformation were inoculated in 1x TE buffer and incubated at 30°C at 180
437 rpm overnight. On the next day, 10 µL of the colonies were spotted on DDO, interaction
438 selective media (triple drop out media: SD/-Leu/-Trp/-His) and triple drop out media
439 containing 2 mM 3-aminotriazole (triple drop out media: SD/-Leu/-Trp/-His/+3-
440 aminotriazole). Pictures were taken 6 days after spotting. SD plates were prepared with 1.6%
441 (w/v) Bactoagar (AppliChem) and the SD media was obtained from TakaraBio**.**

442 **Affinity-based Immunoprecipitation**

443 Proteins were extracted from plant material with RIPA-buffer (50 mM Tris-Cl, pH 7.6, 150
444 mM NaCl, 20 mM NaF, 10 mM $Na_4P_2O_7$, 1 mM EDTA, 0.5 mM EGTA, 1% Nonidet-P-40,
445 0.5% Na-deoxycholate, 1 mM PMSF, 1 mM DTT) for 30 min at 4°C. Post centrifugation the
446 cleared lysate was diluted 1:1 with detergent-free RIPA and incubated with equilibrated GFP-
447 trap or RFP-trap Agarose beads (ChromoTek) for 2h at 8°C on a multi-rotator. After
448 centrifugation (2500xg, 4°C) and washing 3-times (detergent-free RIPA), proteins were eluted
449 at 68°C for 15 min in 2x SDS sample buffer. The supernatant was transferred to a new tube
450 and boiled at 95°C for 5min.

451 **Immunoblotting**

452 Seedlings were germinated on +Pi medium for 5 d prior to transfer to Pi-sufficient (+Pi) or
453 deficient (-Pi) media. Whole roots were harvested 1dpt after treatments. For basal protein

454 quantification whole seedlings were directly harvested 5dpg. Proteins were extracted using
455 RIPA-buffer (50 mM Tris-Cl, pH 7.6, 150 mM NaCl, 20 mM NaF, 10 mM $Na_4P_2O_7$, 1 mM
456 EDTA, 0.5 mM EGTA, 1% Nonidet-P-40, 0.5% Na-deoxycholate, 1 mM PMSF, 1 mM DTT)
457 for 30 min at 4°C. Protein concentrations were measured using the Pierce™ 660 nm Protein-
458 Assay-Kit (Thermo Fisher, 22662). Equal amounts of total proteins were loaded on 10%
459 SDS-gels containing TCE (2,2,2-Trichlorethanol, Sigma-Aldrich, T54801) as loading control
460 (Ladner et al. 2004). All gels were simultaneously immunoblotted. All antibodies used in this
461 study are listed in Supplementary table 3.

462 **Quantitative proteomics**

463 Primary root tips were excised 24 h after transfer to the indicated media and collected into
464 liquid nitrogen. Tissue lysis, sample preparation, protein labeling, Tandem-Mass-Tag (TMT)
465 spectrometry, MS/MS data analysis, and TMT-quantifications were performed as recently
466 described (Naumann et al. 2022; Rodriguez et al. 2020; Stephani et al. 2020).
467 NanoLC-MS/MS Analysis: The nano HPLC system (Vanquish *Neo* UHPLC-System, Thermo
468 Scientific) was coupled to an Orbitrap Astral mass spectrometer, equipped with a Nanospray
469 Flex ion source (all parts Thermo Scientific). Peptides were loaded onto a trap column
470 (PepMap Acclaim C18, 5 mm × 300 µm ID, 5 µm particle size, 100 Å pore size, Thermo
471 Scientific) at a flow rate of 25 µl/min using 0.1% TFA as mobile phase.
472 After 5 minutes, the trap column was switched in line with the analytical column (Aurora
473 Ultimate C18 25cm × 75 µm ID, 1.7 µm particles, 120 Å, with integrated emitter, Ionopticks
474 operated at 50°C). Peptides were eluted using a flow rate of 300 nl/min, starting with the
475 mobile phases 98% A (0.1% formic acid in water) and 2% B (80% acetonitrile, 0.1% formic
476 acid) and linearly increasing to 35% B over the next 60 minutes, followed by an increase to
477 95% B in 1.7 min, a 4-min hold at 95% B, and re-equilibration with 2% B for three column
478 volumes (equilibration factor of 3.0).

479 The Orbitrap Astral was operated in data-dependent mode, performing a full scan in the
480 Orbitrap every 0.7 s (m/z range 375–1500 m/z; resolution 240,000; standard AGC target,
481 maximum injection time 10 ms, minimum intensity 5,000). MS/MS spectra were acquired in
482 the Astral analyser by isolating 1.6 Da windows and fragmenting precursor ions with
483 normalized HCD collision energy of 30% with a maximum injection time of 5 or 10 ms
484 correspondingly or until a standard AGC target was reached. Fragment ions ranging from
485 150–2000 m/z were acquired. Precursor ions selected for fragmentation (include charge state
486 2-6) were put on a dynamic exclusion list for 30 s.

487 **qRT PCR**

488 Abundance of mRNAs was quantified using fluorescence-based real-time RT-PCR and gene-
489 specific amplimers listed in Supplementary table 1. Relative mRNA abundances were
490 normalized relative to *UBC9* transcript abundance. Samples from three independent
491 experiments were measured.

492 **Phylogenetic Analysis**

493 CAN1 sequence alignment and phylogenetic analysis were done using BLAST search of
494 curated sequences in the NCBI database and phytozome 13. Obtained sequences were filtered
495 for fragments. All phylogenetic trees were calculated by sequence alignment using MAFFT
496 7108 with default settings and created at the CIPRES web-portal with RAxML 8.2.10109 for
497 maximum likelihood analyses using the JTT PAM matrix for amino acid substitutions in
498 RAxML. All related sequences used for phylogenetic analyses are provided (Supplementary
499 Data 2).

500 **Quantification and Statistical Analysis**

501 All claims of statistical significance can be found in the corresponding figure legends.
502 Statistical tests were carried out using GraphPad Prism 10 for Windows.

503 **Acknowledgements** We thank P.J. Hussey and P. Wang for seeds; M. Ried and S. Abel for
504 scientific discussions and critical reading of the manuscript. This work was supported by the
505 Deutsche Forschungsgemeinschaft (DFG, German Research Foundation) projects 492493685
506 and 400681449/GRK 2498.; an EMBO Short-Term Fellowship to C.N. and institutional core
507 funding (Leibniz Association) from the Federal Republic of Germany and the State of
508 Saxony-Anhalt. Work in the K.M. group was financially supported by the EPIC-XS (project
509 number 823839), the Horizon 2020 Program of the European Union, and the ERA-CAPS I
510 3686 project of the Austrian Science Fund.

511 **Author contributions** D.G. and C.N. designed research; D.G., F.S., K.M., J.A., F.K., S.M.,
512 Y.TN., N.G. and S.H. conducted experiments and analyzed data; K.M. and R.I. performed
513 proteomic analysis; Y.D. and C.N. supervised the project; D.G. drafted the manuscript; C.N.
514 wrote the article.

515 **Competing interests** The authors declare no competing interests.

516 **LITERATURE CITED**

517 Abel S (2017) Phosphate scouting by root tips. Curr Opin Plant Biol 39:168-177.
518 doi:10.1016/j.pbi.2017.04.016
519 Abel S, Naumann C (2024) Evolution of phosphate scouting in the terrestrial biosphere.
520 Philos Trans R Soc Lond B Biol Sci 379 (1914):20230355.
521 doi:10.1098/rstb.2023.0355
522 Balzergue C, Dartevelle T, Godon C, Laugier E, Meisrimler C, Teulon JM, Creff A, Bissler
523 M, Brouchoud C, Hagege A, Muller J, Chiarenza S, Javot H, Becuwe-Linka N, David
524 P, Peret B, Delannoy E, Thibaud MC, Armengaud J, Abel S, Pellequer JL, Nussaume
525 L, Desnos T (2017) Low phosphate activates STOP1-ALMT1 to rapidly inhibit root
526 cell elongation. Nat Commun 8:15300. doi:10.1038/ncomms15300
527 Cadena-Ramos AI, De-la-Pena C (2024) Picky eaters: selective autophagy in plant cells. Plant
528 J 117 (2):364-384. doi:10.1111/tpj.16508
529 Clua J, Montpetit J, Jimenez-Sandoval P, Naumann C, Santiago J, Poirier Y (2024) A
530 CYBDOM protein impacts iron homeostasis and primary root growth under phosphate
531 deficiency in Arabidopsis. Nat Commun 15 (1):423. doi:10.1038/s41467-023-43911-x
532 Crombez H, Motte H, Beeckman T (2019) Tackling Plant Phosphate Starvation by the Roots.
533 Dev Cell 48 (5):599-615. doi:10.1016/j.devcel.2019.01.002
534 Del Chiaro A, Grujic N, Zhao J, Papareddy RK, Gao P, Ma J, Lofke C, Bhattacharya A,
535 Gruetzner R, Bourguet P, Berger F, Kang BH, Marillonnet S, Dagdas Y (2025)
536 Nonuple atg8 mutant provides genetic evidence for functional specialization of ATG8
537 isoforms in Arabidopsis thaliana. J Cell Sci. doi:10.1242/jcs.263803
538 Dong K, Deng G, Liu Y, Chen KE, Wei H, Huang X, Huang W, Zheng P, Ueda T, Vierstra
539 RD, Huang X, Li F (2025) Comprehensive genetic analyses of Arabidopsis
540 autophagy-related 8 family reveal redundant regulatory roles during autophagy. New
541 Phytol. doi:10.1111/nph.70418
542 Engler C, Youles M, Gruetzner R, Ehnert TM, Werner S, Jones JD, Patron NJ, Marillonnet S
543 (2014) A golden gate modular cloning toolbox for plants. ACS Synth Biol 3 (11):839-
544 843. doi:10.1021/sb4001504
545 Feng Q, De Rycke R, Dagdas Y, Nowack MK (2022) Autophagy promotes programmed cell
546 death and corpse clearance in specific cell types of the Arabidopsis root cap. Curr Biol
547 32 (20):4548. doi:10.1016/j.cub.2022.10.006
548 Feng Z, Zhao Y, Li T, Nie W, Yang X, Wang X, Wu J, Liao J, Zou Y (2020) CATP-8/P5A
549 ATPase Regulates ER Processing of the DMA-1 Receptor for Dendritic Branching.
550 Cell Rep 32 (10):108101. doi:10.1016/j.celrep.2020.108101
551 Gantner J, Ordon J, Ilse T, Kretschmer C, Gruetzner R, Lofke C, Dagdas Y, Burstenbinder K,
552 Marillonnet S, Stuttmann J (2018) Peripheral infrastructure vectors and an extended
553 set of plant parts for the Modular Cloning system. PLoS One 13 (5):e0197185.
554 doi:10.1371/journal.pone.0197185
555 Giehl RF, von Wiren N (2014) Root nutrient foraging. Plant Physiol 166 (2):509-517.
556 doi:10.1104/pp.114.245225
557 Gietz RD, Schiestl RH (2007) High-efficiency yeast transformation using the LiAc/SS carrier
558 DNA/PEG method. Nat Protoc 2 (1):31-34. doi:10.1038/nprot.2007.13
559 Gong F, Yao Z, Liu Y, Sun M, Peng X (2021) H(2)O(2) response gene 1/2 are novel sensors
560 or responders of H(2)O(2) and involve in maintaining embryonic root meristem
561 activity in Arabidopsis thaliana. Plant Sci 310:110981.
562 doi:10.1016/j.plantsci.2021.110981
563 Gross AS, Raffeiner M, Zeng Y, Ustun S, Dagdas Y (2025) Autophagy in Plant Health and
564 Disease. Annu Rev Plant Biol 76 (1):197-227. doi:10.1146/annurev-arplant-060324-
565 094912

566 Gutierrez-Alanis D, Yong-Villalobos L, Jimenez-Sandoval P, Alatorre-Cobos F, Oropeza-
567 Aburto A, Mora-Macias J, Sanchez-Rodriguez F, Cruz-Ramirez A, Herrera-Estrella L
568 (2017) Phosphate Starvation-Dependent Iron Mobilization Induces CLE14 Expression
569 to Trigger Root Meristem Differentiation through CLV2/PEPR2 Signaling. Dev Cell
570 41 (5):555-570 e553. doi:10.1016/j.devcel.2017.05.009
571 Jakobsen MK, Poulsen LR, Schulz A, Fleurat-Lessard P, Moller A, Husted S, Schiott M,
572 Amtmann A, Palmgren MG (2005) Pollen development and fertilization in
573 Arabidopsis is dependent on the MALE GAMETOGENESIS IMPAIRED ANTHERS
574 gene encoding a type V P-type ATPase. Genes Dev 19 (22):2757-2769.
575 doi:10.1101/gad.357305
576 Ji J, Cui MK, Zou R, Wu MZ, Ge MX, Li J, Zhang ZR (2024) An ATP13A1-assisted
577 topogenesis pathway for folding multi-spanning membrane proteins. Mol Cell 84
578 (10):1917-1931 e1915. doi:10.1016/j.molcel.2024.04.010
579 Johansen T, Lamark T (2020) Selective Autophagy: ATG8 Family Proteins, LIR Motifs and
580 Cargo Receptors. J Mol Biol 432 (1):80-103. doi:10.1016/j.jmb.2019.07.016
581 Jung H, Lee HN, Marshall RS, Lomax AW, Yoon MJ, Kim J, Kim JH, Vierstra RD, Chung T
582 (2020) Arabidopsis cargo receptor NBR1 mediates selective autophagy of defective
583 proteins. J Exp Bot 71 (1):73-89. doi:10.1093/jxb/erz404
584 Kellermeier F, Armengaud P, Seditas TJ, Danku J, Salt DE, Amtmann A (2014) Analysis of
585 the Root System Architecture of Arabidopsis Provides a Quantitative Readout of
586 Crosstalk between Nutritional Signals. Plant Cell 26 (4):1480-1496.
587 doi:10.1105/tpc.113.122101
588 L. Franke BS, J. L. Erickson, D. Rödel, D. Schröter, B. Möller, and M. H. Schattat (2015) The
589 'MTB Cell Counter' a versatile tool for the semi-automated quantification of sub-
590 cellular phenotypes in fluorescence microscopy images. A case study on plastids,
591 nuclei and peroxisomes. Journal of Endocytobiosis and Cell Research 26:31-42
592 Labun K, Montague TG, Krause M, Torres Cleuren YN, Tjeldnes H, Valen E (2019)
593 CHOPCHOP v3: expanding the CRISPR web toolbox beyond genome editing.
594 Nucleic Acids Res 47 (W1):W171-W174. doi:10.1093/nar/gkz365
595 Ladner CL, Yang J, Turner RJ, Edwards RA (2004) Visible fluorescent detection of proteins
596 in polyacrylamide gels without staining. Anal Biochem 326 (1):13-20.
597 doi:10.1016/j.ab.2003.10.047
598 Lai Z, Wang F, Zheng Z, Fan B, Chen Z (2011) A critical role of autophagy in plant
599 resistance to necrotrophic fungal pathogens. Plant J 66 (6):953-968.
600 doi:10.1111/j.1365-313X.2011.04553.x
601 Lambers H, Martinoia E, Renton M (2015) Plant adaptations to severely phosphorus-
602 impoverished soils. Curr Opin Plant Biol 25:23-31. doi:10.1016/j.pbi.2015.04.002
603 Lerouxel O, Mouille G, Andeme-Onzighi C, Bruyant MP, Seveno M, Loutelier-Bourhis C,
604 Driouich A, Hofte H, Lerouge P (2005) Mutants in DEFECTIVE
605 GLYCOSYLATION, an Arabidopsis homolog of an oligosaccharyltransferase
606 complex subunit, show protein underglycosylation and defects in cell differentiation
607 and growth. Plant J 42 (4):455-468. doi:10.1111/j.1365-313X.2005.02392.x
608 Li C, Duckney P, Zhang T, Fu Y, Li X, Kroon J, De Jaeger G, Cheng Y, Hussey PJ, Wang P
609 (2022) TraB family proteins are components of ER-mitochondrial contact sites and
610 regulate ER-mitochondrial interactions and mitophagy. Nat Commun 13 (1):5658.
611 doi:10.1038/s41467-022-33402-w
612 Li P, Bagenholm V, Hagglund P, Lindkvist-Petersson K, Wang K, Gourdon P (2024) The
613 structure and function of P5A-ATPases. Nat Commun 15 (1):9605.
614 doi:10.1038/s41467-024-53757-6

615 Li T, Yang X, Feng Z, Nie W, Fang Z, Zou Y (2021) P5A ATPase controls ER translocation
616 of Wnt in neuronal migration. Cell Rep 37 (4):109901.
617 doi:10.1016/j.celrep.2021.109901
618 Limpens E, Ramos J, Franken C, Raz V, Compaan B, Franssen H, Bisseling T, Geurts R
619 (2004) RNA interference in Agrobacterium rhizogenes-transformed roots of
620 Arabidopsis and Medicago truncatula. J Exp Bot 55 (399):983-992.
621 doi:10.1093/jxb/erh122
622 Liu F, Hu W, Li F, Marshall RS, Zarza X, Munnik T, Vierstra RD (2020) AUTOPHAGY-
623 RELATED14 and Its Associated Phosphatidylinositol 3-Kinase Complex Promote
624 Autophagy in Arabidopsis. Plant Cell 32 (12):3939-3960. doi:10.1105/tpc.20.00285
625 Liu W, Liu Z, Mo Z, Guo S, Liu Y, Xie Q (2021) ATG8-Interacting Motif: Evolution and
626 Function in Selective Autophagy of Targeting Biological Processes. Front Plant Sci
627 12:783881. doi:10.3389/fpls.2021.783881
628 Liu Y, Bassham DC (2012) Autophagy: pathways for self-eating in plant cells. Annu Rev
629 Plant Biol 63:215-237. doi:10.1146/annurev-arplant-042811-105441
630 Man Y, Zhang Y, Chen L, Zhou J, Bu Y, Zhang X, Li X, Li Y, Jing Y, Lin J (2024) The
631 VAMP-associated protein VAP27-1 plays a crucial role in plant resistance to ER
632 stress by modulating ER-PM contact architecture in Arabidopsis. Plant Commun 5
633 (7):100929. doi:10.1016/j.xplc.2024.100929
634 Maniero RA, Picco C, Hartmann A, Engelberger F, Gradogna A, Scholz-Starke J, Melzer M,
635 Kunze G, Carpaneto A, von Wiren N, Giehl RFH (2024) Ferric reduction by a
636 CYBDOM protein counteracts increased iron availability in root meristems induced
637 by phosphorus deficiency. Nat Commun 15 (1):422. doi:10.1038/s41467-023-43912-
638 w
639 McKenna MJ, Adams BM, Chu V, Paulo JA, Shao S (2022) ATP13A1 prevents ERAD of
640 folding-competent mislocalized and misoriented proteins. Mol Cell 82 (22):4277-4289
641 e4210. doi:10.1016/j.molcel.2022.09.035
642 McKenna MJ, Sim SI, Ordureau A, Wei L, Harper JW, Shao S, Park E (2020) The
643 endoplasmic reticulum P5A-ATPase is a transmembrane helix dislocase. Science 369
644 (6511). doi:10.1126/science.abc5809
645 Muller J, Toev T, Heisters M, Teller J, Moore KL, Hause G, Dinesh DC, Burstenbinder K,
646 Abel S (2015) Iron-dependent callose deposition adjusts root meristem maintenance to
647 phosphate availability. Dev Cell 33 (2):216-230. doi:10.1016/j.devcel.2015.02.007
648 Nakatogawa H (2020) Mechanisms governing autophagosome biogenesis. Nat Rev Mol Cell
649 Biol 21 (8):439-458. doi:10.1038/s41580-020-0241-0
650 Nascimbeni AC, Codogno P, Morel E (2017) Phosphatidylinositol-3-phosphate in the
651 regulation of autophagy membrane dynamics. FEBS J 284 (9):1267-1278.
652 doi:10.1111/febs.13987
653 Naumann C, Heisters M, Brandt W, Janitza P, Alfs C, Tang N, Toto Nienguesso A, Ziegler J,
654 Imre R, Mechtler K, Dagdas Y, Hoehenwarter W, Sawers G, Quint M, Abel S (2022)
655 Bacterial-type ferroxidase tunes iron-dependent phosphate sensing during Arabidopsis
656 root development. Curr Biol 32 (10):2189-2205 e2186. doi:10.1016/j.cub.2022.04.005
657 Naumann C, Muller J, Sakhonwasee S, Wieghaus A, Hause G, Heisters M, Burstenbinder K,
658 Abel S (2019) The Local Phosphate Deficiency Response Activates Endoplasmic
659 Reticulum Stress-Dependent Autophagy. Plant Physiol 179 (2):460-476.
660 doi:10.1104/pp.18.01379
661 Nthiga TM, Kumar Shrestha B, Sjottem E, Bruun JA, Bowitz Larsen K, Bhujabal Z, Lamark
662 T, Johansen T (2020) CALCOCO1 acts with VAMP-associated proteins to mediate
663 ER-phagy. EMBO J 39 (15):e103649. doi:10.15252/embj.2019103649

664 Ordon J, Gantner J, Kemna J, Schwalgun L, Reschke M, Streubel J, Boch J, Stuttmann J
665 (2017) Generation of chromosomal deletions in dicotyledonous plants employing a
666 user-friendly genome editing toolkit. Plant J 89 (1):155-168. doi:10.1111/tpj.13319
667 Petersen M, Avin-Wittenberg T, Bassham DC, Dagdas Y, Fan C, Fernie AR, Jiang L, Mishra
668 D, Otegui MS, Rodriguez E, Hofius D (2024) Autophagy in plants. Autophagy Rep 3
669 (1):2395731. doi:10.1080/27694127.2024.2395731
670 Picchianti L, Sanchez de Medina Hernandez V, Zhan N, Irwin NA, Groh R, Stephani M,
671 Hornegger H, Beveridge R, Sawa-Makarska J, Lendl T, Grujic N, Naumann C,
672 Martens S, Richards TA, Clausen T, Ramundo S, Karagoz GE, Dagdas Y (2023)
673 Shuffled ATG8 interacting motifs form an ancestral bridge between UFMylation and
674 autophagy. EMBO J 42 (10):e112053. doi:10.15252/embj.2022112053
675 Qi H, Wang Y, Bao Y, Bassham DC, Chen L, Chen QF, Hou S, Hwang I, Huang L, Lai Z, Li
676 F, Liu Y, Qiu R, Wang H, Wang P, Xie Q, Zeng Y, Zhuang X, Gao C, Jiang L, Xiao S
677 (2023) Studying plant autophagy: challenges and recommended methodologies. Adv
678 Biotechnol (Singap) 1 (4):2. doi:10.1007/s44307-023-00002-8
679 Qin Q, Zhao T, Zou W, Shen K, Wang X (2020) An Endoplasmic Reticulum ATPase
680 Safeguards Endoplasmic Reticulum Identity by Removing Ectopically Localized
681 Mitochondrial Proteins. Cell Rep 33 (6):108363. doi:10.1016/j.celrep.2020.108363
682 Rodriguez E, Chevalier J, Olsen J, Ansbol J, Kapousidou V, Zuo Z, Svenning S, Loefke C,
683 Koemeda S, Drozdowskyj PS, Jez J, Durnberger G, Kuenzl F, Schutzbier M, Mechtler
684 K, Ebstrup EN, Lolle S, Dagdas Y, Petersen M (2020) Autophagy mediates temporary
685 reprogramming and dedifferentiation in plant somatic cells. EMBO J 39 (4):e103315.
686 doi:10.15252/embj.2019103315
687 Rogov VV, Nezis IP, Tsapras P, Zhang H, Dagdas Y, Noda NN, Nakatogawa H, Wirth M,
688 Mouilleron S, McEwan DG, Behrends C, Deretic V, Elazar Z, Tooze SA, Dikic I,
689 Lamark T, Johansen T (2023) Atg8 family proteins, LIR/AIM motifs and other
690 interaction modes. Autophagy Rep 2 (1). doi:10.1080/27694127.2023.2188523
691 Schindelin J, Arganda-Carreras I, Frise E, Kaynig V, Longair M, Pietzsch T, Preibisch S,
692 Rueden C, Saalfeld S, Schmid B, Tinevez JY, White DJ, Hartenstein V, Eliceiri K,
693 Tomancak P, Cardona A (2012) Fiji: an open-source platform for biological-image
694 analysis. Nat Methods 9 (7):676-682. doi:10.1038/nmeth.2019
695 Shen J, Yuan L, Zhang J, Li H, Bai Z, Chen X, Zhang W, Zhang F (2011) Phosphorus
696 dynamics: from soil to plant. Plant Physiol 156 (3):997-1005.
697 doi:10.1104/pp.111.175232
698 Shin KD, Lee HN, Chung T (2014) A revised assay for monitoring autophagic flux in
699 Arabidopsis thaliana reveals involvement of AUTOPHAGY-RELATED9 in
700 autophagy. Mol Cells 37 (5):399-405. doi:10.14348/molcells.2014.0042
701 Sim SI, Park E (2023) P5-ATPases: Structure, substrate specificities, and transport
702 mechanisms. Curr Opin Struct Biol 79:102531. doi:10.1016/j.sbi.2023.102531
703 Stefano G, Renna L, Wormsbaecher C, Gamble J, Zienkiewicz K, Brandizzi F (2018) Plant
704 Endocytosis Requires the ER Membrane-Anchored Proteins VAP27-1 and VAP27-3.
705 Cell Rep 23 (8):2299-2307. doi:10.1016/j.celrep.2018.04.091
706 Stephani M, Dagdas Y (2020) Plant Selective Autophagy-Still an Uncharted Territory With a
707 Lot of Hidden Gems. J Mol Biol 432 (1):63-79. doi:10.1016/j.jmb.2019.06.028
708 Stephani M, Picchianti L, Dagdas Y (2021) C53 is a cross-kingdom conserved reticulophagy
709 receptor that bridges the gap betweenselective autophagy and ribosome stalling at the
710 endoplasmic reticulum. Autophagy 17 (2):586-587.
711 doi:10.1080/15548627.2020.1846304
712 Stephani M, Picchianti L, Gajic A, Beveridge R, Skarwan E, Sanchez de Medina Hernandez
713 V, Mohseni A, Clavel M, Zeng Y, Naumann C, Matuszkiewicz M, Turco E, Loefke C,
714 Li B, Durnberger G, Schutzbier M, Chen HT, Abdrakhmanov A, Savova A, Chia KS,

715 Djamei A, Schaffner I, Abel S, Jiang L, Mechtler K, Ikeda F, Martens S, Clausen T,
716 Dagdas Y (2020) A cross-kingdom conserved ER-phagy receptor maintains
717 endoplasmic reticulum homeostasis during stress. Elife 9. doi:10.7554/eLife.58396
718 Stuttmann J, Barthel K, Martin P, Ordon J, Erickson JL, Herr R, Ferik F, Kretschmer C,
719 Berner T, Keilwagen J, Marillonnet S, Bonas U (2021) Highly efficient multiplex
720 editing: one-shot generation of 8x Nicotiana benthamiana and 12x Arabidopsis
721 mutants. Plant J 106 (1):8-22. doi:10.1111/tpj.15197
722 Su T, Li X, Yang M, Shao Q, Zhao Y, Ma C, Wang P (2020) Autophagy: An Intracellular
723 Degradation Pathway Regulating Plant Survival and Stress Response. Front Plant Sci
724 11:164. doi:10.3389/fpls.2020.00164
725 Suzuki NN, Yoshimoto K, Fujioka Y, Ohsumi Y, Inagaki F (2005) The crystal structure of
726 plant ATG12 and its biological implication in autophagy. Autophagy 1 (2):119-126.
727 doi:10.4161/auto.1.2.1859
728 Svenning S, Lamark T, Krause K, Johansen T (2011) Plant NBR1 is a selective autophagy
729 substrate and a functional hybrid of the mammalian autophagic adapters NBR1 and
730 p62/SQSTM1. Autophagy 7 (9):993-1010. doi:10.4161/auto.7.9.16389
731 Svistoonoff S, Creff A, Reymond M, Sigoillot-Claude C, Ricaud L, Blanchet A, Nussaume L,
732 Desnos T (2007) Root tip contact with low-phosphate media reprograms plant root
733 architecture. Nat Genet 39 (6):792-796. doi:10.1038/ng2041
734 Thompson AR, Doelling JH, Suttangkakul A, Vierstra RD (2005) Autophagic nutrient
735 recycling in Arabidopsis directed by the ATG8 and ATG12 conjugation pathways.
736 Plant Physiol 138 (4):2097-2110. doi:10.1104/pp.105.060673
737 Ticconi CA, Delatorre CA, Abel S (2001) Attenuation of phosphate starvation responses by
738 phosphite in Arabidopsis. Plant Physiol 127 (3):963-972
739 Ticconi CA, Lucero RD, Sakhonwasee S, Adamson AW, Creff A, Nussaume L, Desnos T,
740 Abel S (2009) ER-resident proteins PDR2 and LPR1 mediate the developmental
741 response of root meristems to phosphate availability. Proc Natl Acad Sci U S A 106
742 (33):14174-14179. doi:10.1073/pnas.0901778106
743 Walczak M, Martens S (2013) Dissecting the role of the Atg12-Atg5-Atg16 complex during
744 autophagosome formation. Autophagy 9 (3):424-425. doi:10.4161/auto.22931
745 Wang P, Pleskot R, Zang J, Winkler J, Wang J, Yperman K, Zhang T, Wang K, Gong J, Guan
746 Y, Richardson C, Duckney P, Vandorpe M, Mylle E, Fiserova J, Van Damme D,
747 Hussey PJ (2019) Plant AtEH/Pan1 proteins drive autophagosome formation at ER-
748 PM contact sites with actin and endocytic machinery. Nat Commun 10 (1):5132.
749 doi:10.1038/s41467-019-12782-6
750 Wang P, Richardson C, Hawkins TJ, Sparkes I, Hawes C, Hussey PJ (2016) Plant VAP27
751 proteins: domain characterization, intracellular localization and role in plant
752 development. New Phytol 210 (4):1311-1326. doi:10.1111/nph.13857
753 Wang Y, Nishimura MT, Zhao T, Tang D (2011) ATG2, an autophagy-related protein,
754 negatively affects powdery mildew resistance and mildew-induced cell death in
755 Arabidopsis. Plant J 68 (1):74-87. doi:10.1111/j.1365-313X.2011.04669.x
756 Weber E, Engler C, Gruetzner R, Werner S, Marillonnet S (2011) A modular cloning system
757 for standardized assembly of multigene constructs. PLoS One 6 (2):e16765.
758 doi:10.1371/journal.pone.0016765
759 Wild P, McEwan DG, Dikic I (2014) The LC3 interactome at a glance. J Cell Sci 127 (Pt
760 1):3-9. doi:10.1242/jcs.140426
761 Wilfling F, Lee CW, Erdmann PS, Zheng Y, Sherpa D, Jentsch S, Pfander B, Schulman BA,
762 Baumeister W (2020) A Selective Autophagy Pathway for Phase-Separated Endocytic
763 Protein Deposits. Mol Cell 80 (5):764-778 e767. doi:10.1016/j.molcel.2020.10.030

764 Yang SY, Lin WY, Hsiao YM, Chiou TJ (2024) Milestones in understanding transport,
765 sensing, and signaling of the plant nutrient phosphorus. Plant Cell 36 (5):1504-1523.
766 doi:10.1093/plcell/koad326
767 Yoshitake Y, Nakamura S, Shinozaki D, Izumi M, Yoshimoto K, Ohta H, Shimojima M
768 (2021) RCB-mediated chlorophagy caused by oversupply of nitrogen suppresses
769 phosphate-starvation stress in plants. Plant Physiol 185 (2):318-330.
770 doi:10.1093/plphys/kiaa030
771 Yoshitake Y, Shinozaki D, Yoshimoto K (2022) Autophagy triggered by iron-mediated ER
772 stress is an important stress response to the early phase of Pi starvation in plants. Plant
773 J 110 (5):1370-1381. doi:10.1111/tpj.15743
774 Zhao D, Zou CX, Liu XM, Jiang ZD, Yu ZQ, Suo F, Du TY, Dong MQ, He W, Du LL (2020)
775 A UPR-Induced Soluble ER-Phagy Receptor Acts with VAPs to Confer ER Stress
776 Resistance. Mol Cell 79 (6):963-977 e963. doi:10.1016/j.molcel.2020.07.019
777 Zhao J, Bui MT, Ma J, Kunzl F, Picchianti L, De La Concepcion JC, Chen Y, Petsangouraki
778 S, Mohseni A, Garcia-Leon M, Gomez MS, Giannini C, Gwennogan D, Kobylinska
779 R, Clavel M, Schellmann S, Jaillais Y, Friml J, Kang BH, Dagdas Y (2022) Plant
780 autophagosomes mature into amphisomes prior to their delivery to the central vacuole.
781 J Cell Biol 221 (12). doi:10.1083/jcb.202203139
782 Zheng X, Zhao C, Liu Y (2018) Examining Autophagy in Plant by Transmission Electron
783 Microscopy (TEM). Bio Protoc 8 (20):e3047. doi:10.21769/BioProtoc.3047
784 Zhuang X, Wang H, Lam SK, Gao C, Wang X, Cai Y, Jiang L (2013) A BAR-domain protein
785 SH3P2, which binds to phosphatidylinositol 3-phosphate and ATG8, regulates
786 autophagosome formation in Arabidopsis. Plant Cell 25 (11):4596-4615.
787 doi:10.1105/tpc.113.118307

Figure 1

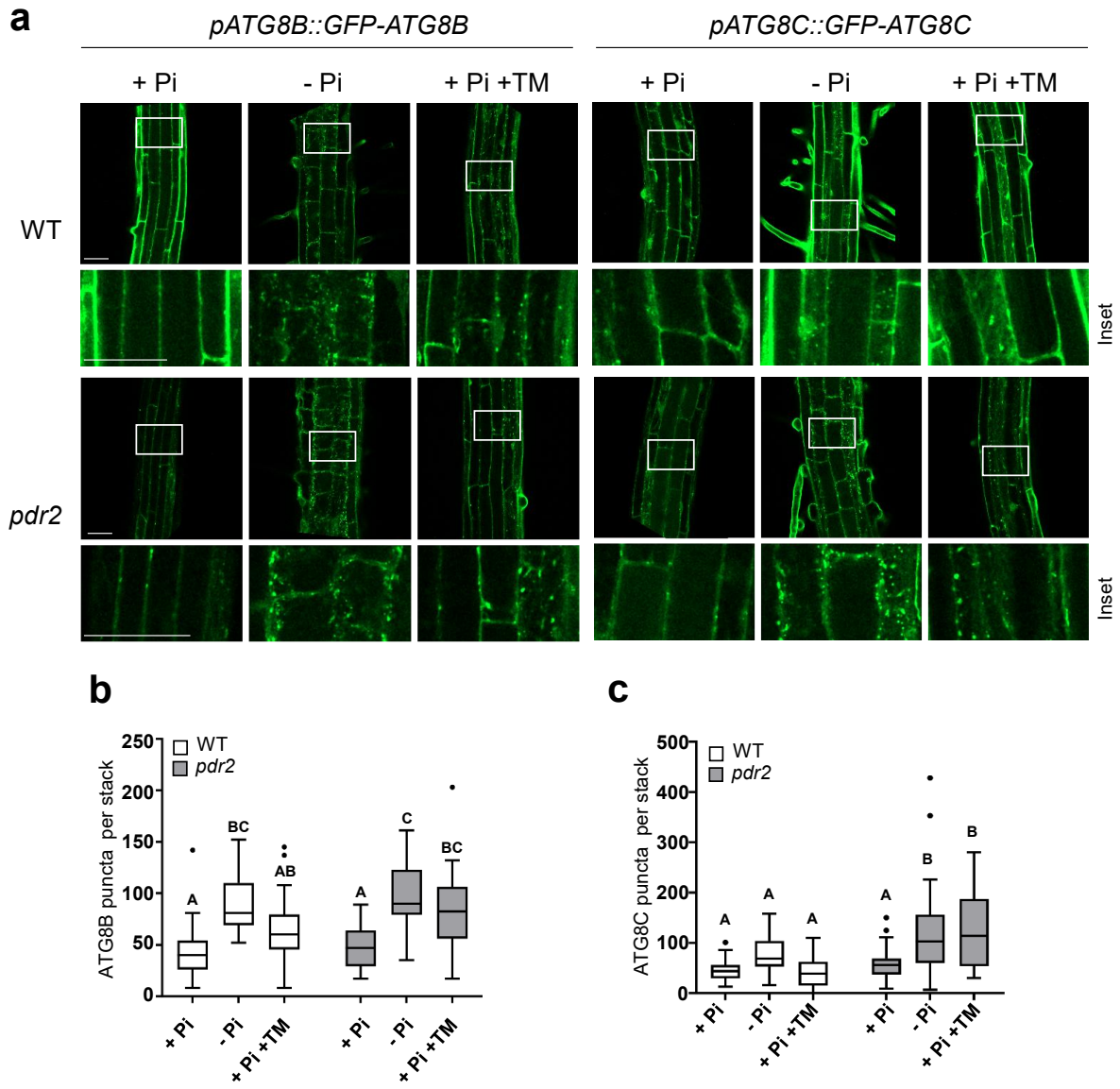

Figure 1: ER stress-induced autophagy by local Pi-sensing specifically activates ATG8B and ATG8C decorated autophagosomes. a, GFP-ATG8B and C labeled autophagosomes in Pi-deprived root tips. GFP-ATG8B/C derived fluorescence in primary root tips of transgenic (*pATG8B/C::GFP-ATG8B/C*) wildtype and *pdr2* seedlings after germination on +Pi agar (5 d) and subsequent transfer to –Pi medium for 0-24 h or treatment with 5 µg/mL tunicamycin (TM) for 6 h. Shown are representative images from three independent experiments fused Z-stacks of the transition zone. Rectangle indicate inset selection. Scale bars, 50 µm. **b** and **c**, Quantification of dataset shown in (**a**). Quantification of GFP-ATG8 puncta in root cells per normalized area. Box plots show medians and interquartile ranges of detected autophagosomes; outliers (>1.53 interquartile range) are shown as black dots. Letters denote statistical differences in condition at $p < 0.05$ (Two-way ANOVA and Tukey's HSD post hoc test) and $n \geq 27$.

Figure 2

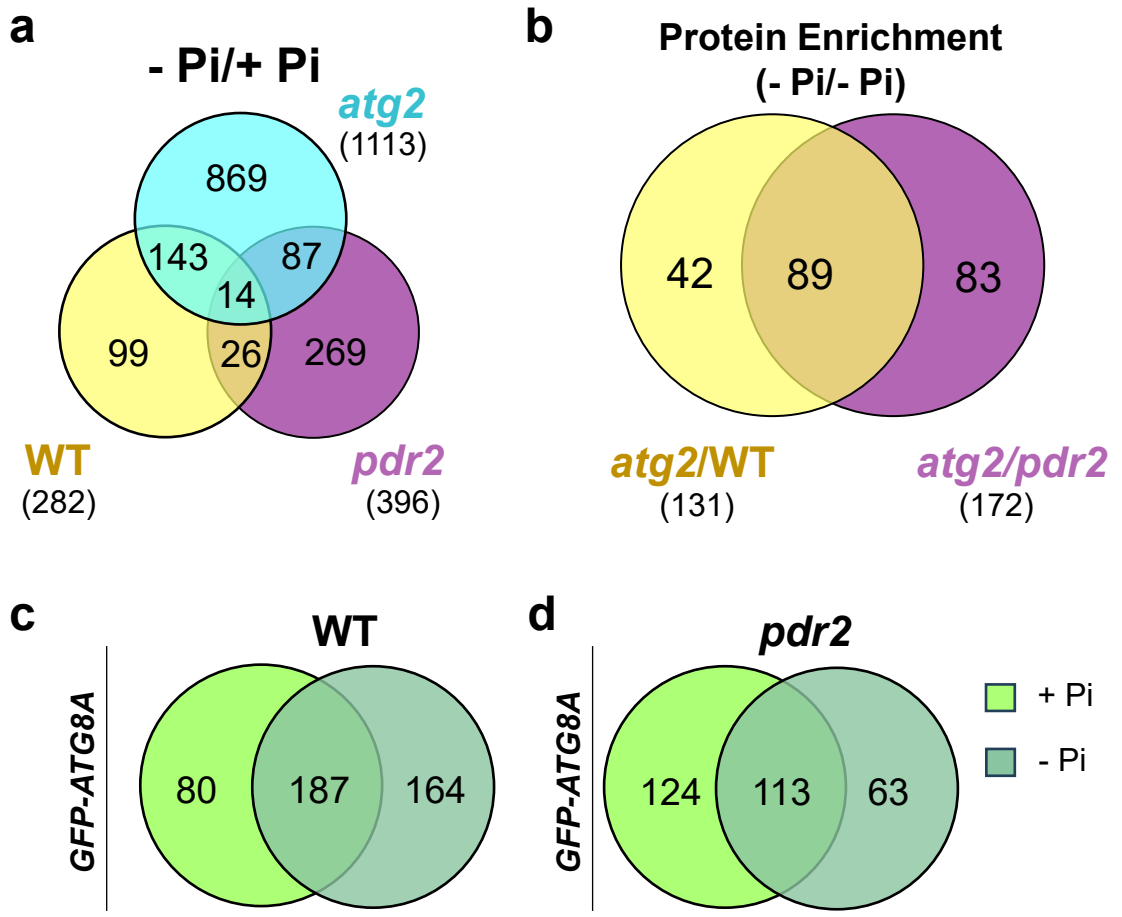

e

Fold Change		ATG8 Interaction		ID	name
WT	*pdr2*	WT	*pdr2*		
3.52	**3.67**	yes	yes	AT5G40690.1	CAN1
2.40	**2.33**	yes	yes	AT4G04620.2	ATG8B
1.91	**1.88**	yes	yes	AT1G62040.2	ATG8C
1.81	1.78	yes	yes	AT1G44770.1	unknown protein
1.72	1.76	yes	yes	AT4G24690.1	NBR1
1.33	1.35	yes	yes	AT3G49490.1	unknown protein

Figure 2: Autophagy modulates root tip proteome composition. a, Seedlings were germinated 5 days prior to transfer to the indicated treatments. 24 h post transfer primary root tips were excised and either directly subjected to extraction and quantification by mass-spectrometry (TMT-analysis) or used for co-immunoprecipitation followed by MS analysis. Venn diagram of three overlapping pairwise comparisons for root tip TMT-MS conducted in wildtype (yellow), *pdr2* (magenta) and *atg2* (cyan) plants: wildtype (-Pi) vs wildtype (+Pi) yellow cycle, *pdr2* (-Pi) vs. *pdr2* (+Pi) magenta cycle, *atg2* (-Pi) vs. *atg2* (+Pi) cyan cycle. Protein abundances with 0.6 > FC > 1.3. Total numbers are depicted in brackets. **b**, Overlap between proteins detected in –Pi conditions enriched in *atg2* compared to wildtype (yellow) or *pdr2-1* (magenta) identified by quantitative MS, FC > 1.3. Intersections show proteins with increased abundance in *atg2* but not in wildtype or *pdr2-1*. **c**,**d** *In vitro* interactome of GFP-ATG8A. Root extracts of GFP-ATG8A in transgenic wildtype (WT, **c**) and *pdr2* (**d**) primary roots were incubated with GFP-Trap beads and interacting proteins were analyzed by MS.

Venn diagram of proteins co-eluting with GFP-ATG8A in +Pi (light green) and -Pi (dark green) according to the genotype. **e**, Summarized results of data obtained in c and d. Fold-Change (log2) of normalized protein abundances in *atg2* compared to wildtype (first column) and *pdr2* (second column) in -Pi conditions.

Figure 3

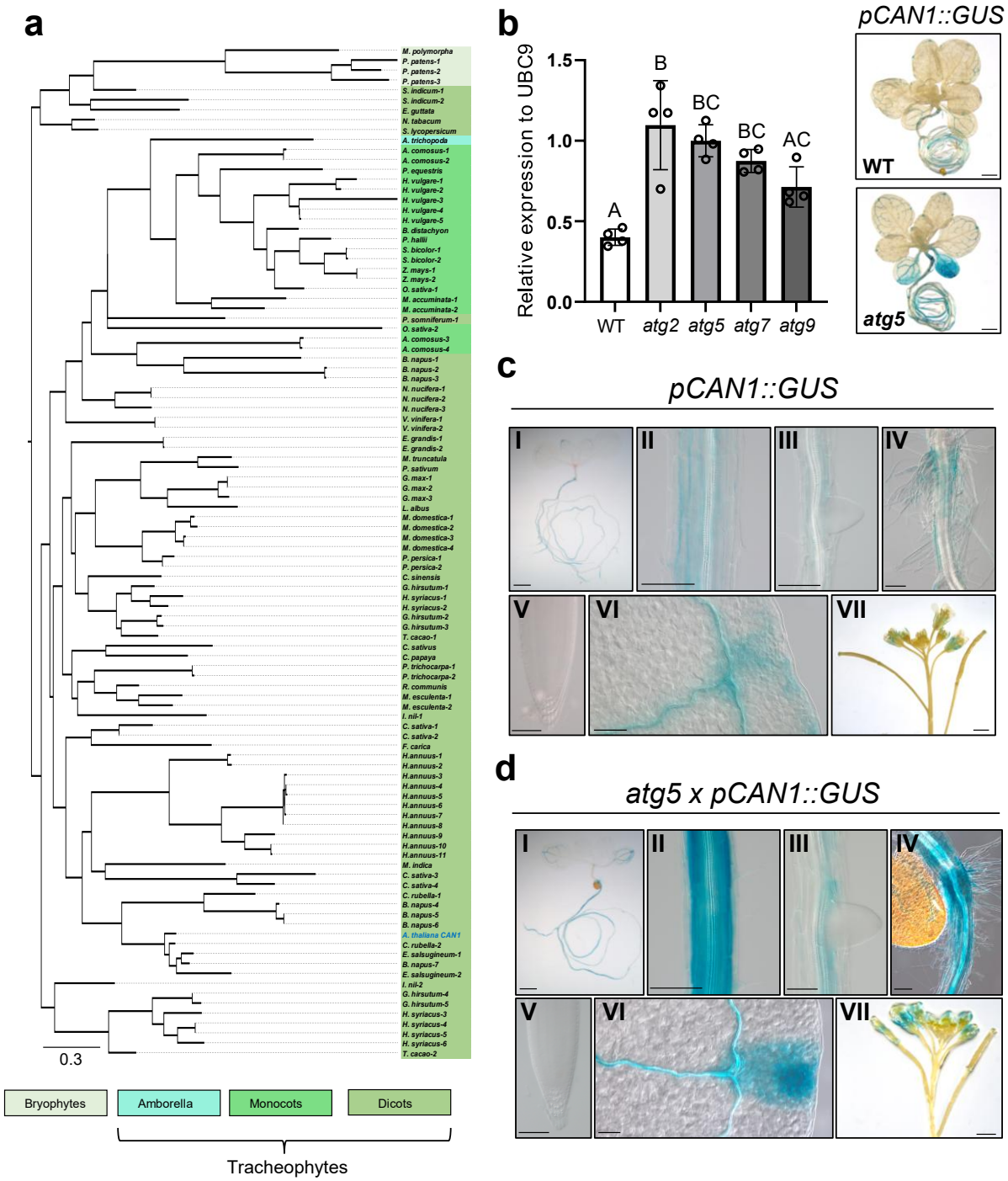

Figure 3: CAN1 is a plant specific protein. a, Maximum-likelihood midpoint-rooted tree (400 bootstrap replicates) of full-length CAN1 orthologues (see Supplementary Data 2). **b-d**, *CAN1* gene is predominantly expressed in root tissue and elevated in autophagy mutant plants. **b**, Left panel: RT-qPCR analysis of *CAN1* transcript abundance relative to *UBC9* in seedlings of wildtype, *atg2*, *atg5*, *atg7* and *atg9,* n = 4; right panel: *pCAN1::GUS* activity in 3 week old seedlings of wildtype and *atg5,* scale bar 1 cm. **c,d**, *pCAN1::GUS* activity in 7 days old wildtype (c) and *atg5* (d) seedlings (I), root elongation zone (II), lateral root emergence (III), root-shoot junction (IV), primary root tip (V), true leaf tip (VI) and flower (VII), I-VI scale bar 100 µm, VII scale bar 1 cm, n ≥ 8.

Figure 4

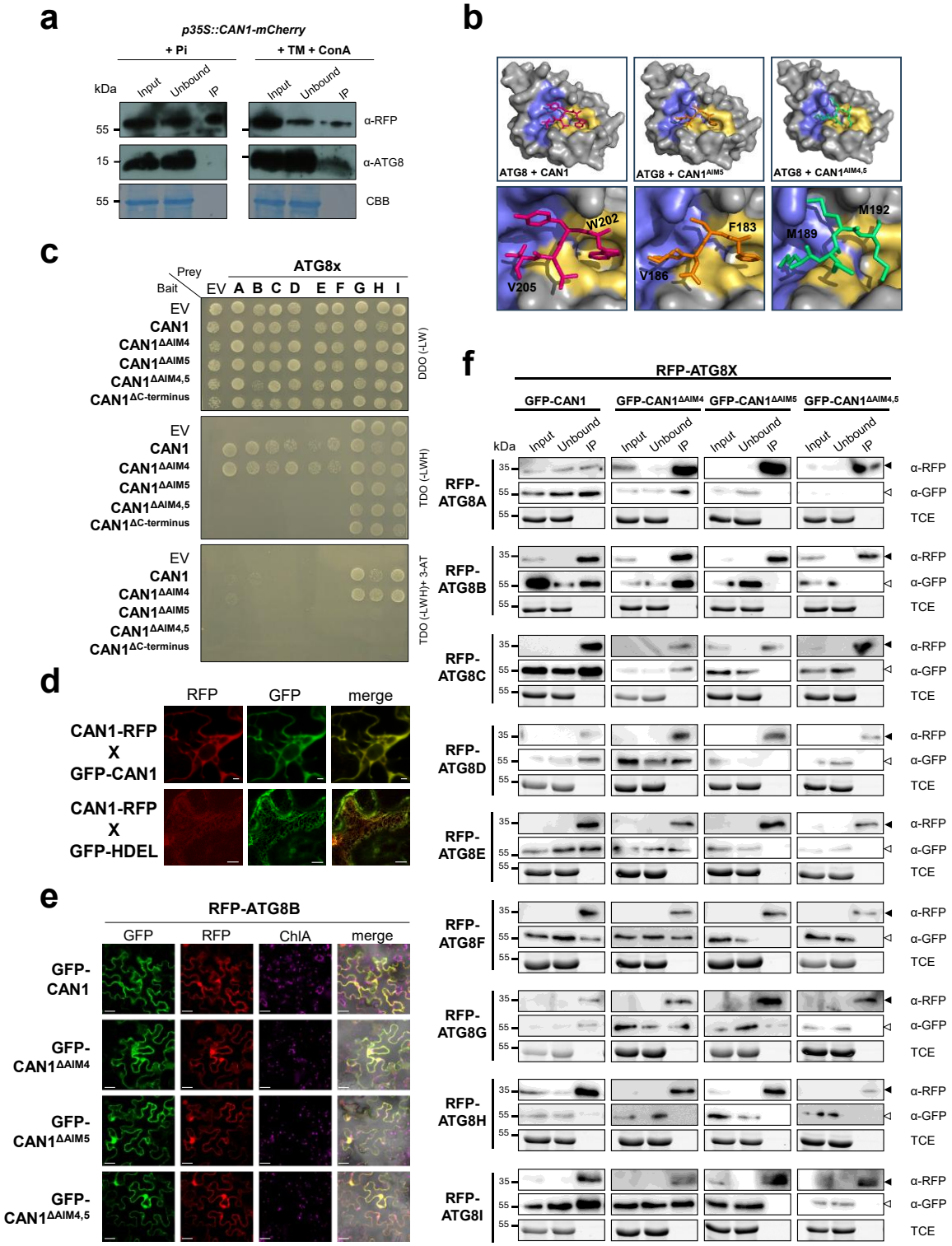

Figure 4: CAN1 interacts with ATG8 isoforms via select AIMs. a, endogenous ATG8 interacts with CAN1. *In vivo* immunoprecipitation of extracts of Arabidopsis seedlings expressing CAN1-mCherry after germination on + Pi media for 5 days. ER stress was applied by incubation in +Pi with 5 µg/mL TM and 1 µM ConA containing liquid media for 7h. Input and bound proteins were visualized by immunoblotting with anti-RFP and anti-ATG8 antibodies, loading control Coomassie blue staining (CBB). **b**, Colabfold prediction of CAN1-ATG8 interaction via AIM4 and AIM5. *In silico* prediction of CAN1 interaction with ATG8E

revealed interaction via AIM5 (stick representation; see also Figure S6) which locates in Arabidopsis ATG8E (surface representation–grey) AIM pockets, known as W-site (site 1 – yellow) and L-site (site 2 –slate blue) (top panel) interacting with W202 and V205 (top right panel, close view – red). *In silico* mutation of W202A and V205A (CAN1$^{\Delta AIM5}$) predicts ATG8E CAN1 interaction via AIM4 (middle panel, right close view –orange) with F183 and V186 interacting with site 1 and site 2 respectively. CAN1 depleted of AIM4 and AIM5 is not predicted to interact with ATG8E via the AIM pockets (lower row panels, CAN1 $^{\Delta AIM4/5}$ – green). **c**, CAN1 interacts AIM specific *in vivo*. Y2H assay between a GAL4 DNA binding domain (DBD, bait) fused variant of CAN1 with GAL4 activation domain (AD, prey) fused variants of all nine ATG8 isoforms A-I. GAL4-DBD and AD alone were included as negative controls (EV). The growth of yeast cultures on vector-selective (−Trp/−Leu) (top), interaction-selective (−Trp/−Leu/−His) (middle) and strong interaction-selective (−Trp/−Leu/−His + 3-aminotriazol) media (bottom) six days after spotting is shown. **d**, Subcellular localization of CAN1-RFP. Co-expression of CAN1-RFP with GFP-CAN1 (Upper row) or GFP-HDEL (lower row) in transient expression assays in *N. benthamiana*. The images are single optical sections of RFP (left column), GFP (center column) and merged signals (right column). Scale bars, 10 µm. **e**,**f** CAN1 interacts with ATG8 in an isoform and AIM specific manner. **e**, Localization of GFP-CAN1 variants (CAN1, CAN1$^{\Delta AIM4}$, CAN1$^{\Delta AIM5}$ CAN1$^{\Delta AIM4/5}$) transiently co-expressed with RFP-ATG8B in *N. benthamiana*. The images are single optical sections of GFP (first column), RFP (second column), chlorophyll A (third column, blue) and merged (including bright field) signals (last column). Scale bars, 30 µm, n = 3. **f**, *In vitro* co-immunoprecipitation assays of all nine RFP-ATG8x isoforms co-expressed with CAN1-GFP variants in *N. benthamiana* via RFP-Trap. Presence of RFP-ATG8A-I and GFP-CAN1 variants was visualized by immunoblotting with anti-RFP and anti-GFP antibodies, loading control TCE visualization, n = 5.

Figure 5

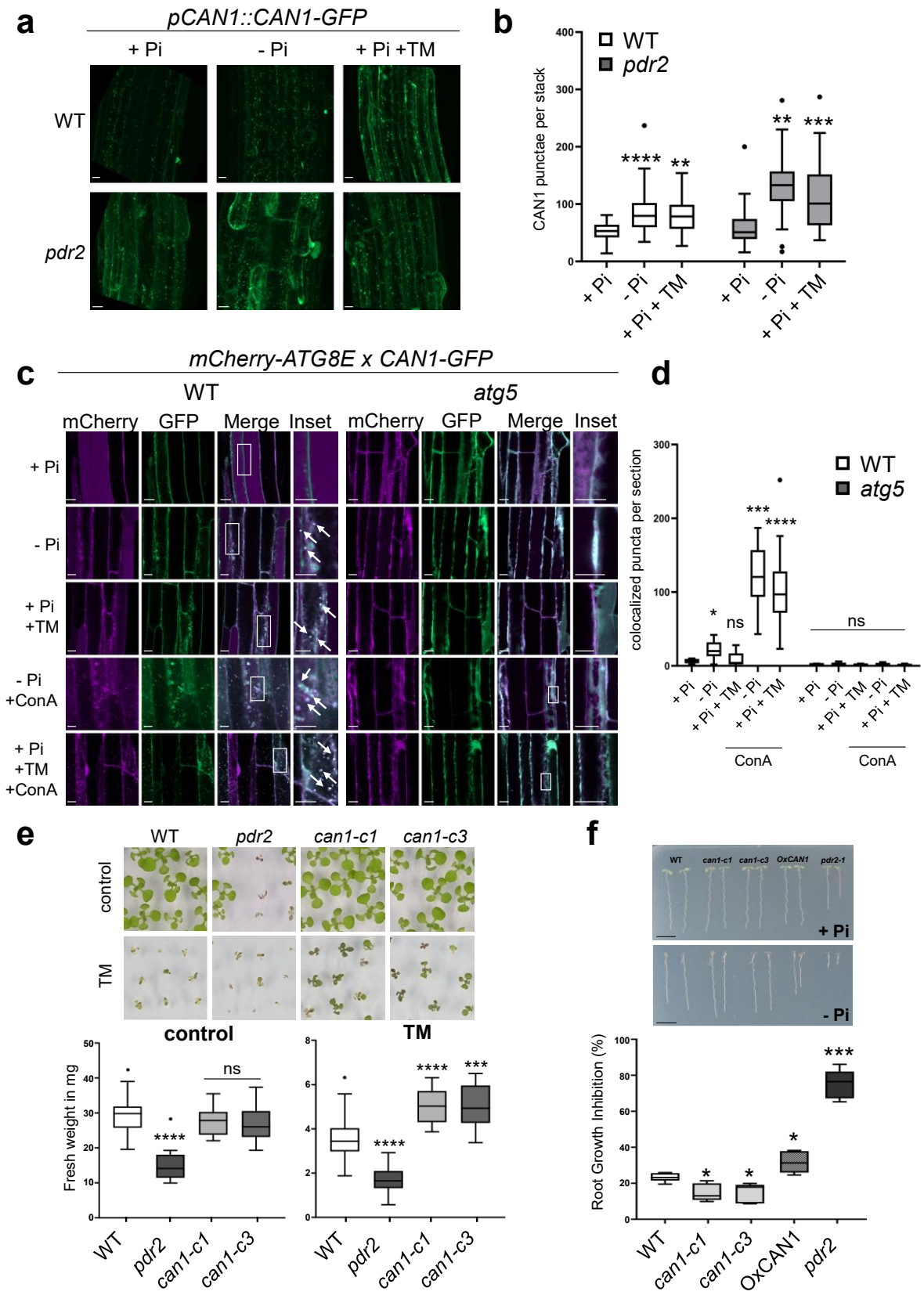

Figure 5: CAN1 functions in Pi-dependent ER stress-induced autophagy. a, CAN1-GFP derived fluorescence in the transition zone of transgenic (*pCAN1::CAN1-GFP*) wildtype and *pdr2* seedlings after germination on +Pi agar (5 d) and subsequent transfer to + or –Pi medium

for 24 h or treatment with TM in liquid + Pi media for 6 h. Shown are representative images from three independent experiments fused Z-stacks of the root tip. Scale bars, 20 µm. **b**, Quantification of CAN1-GFP puncta in root cells per area. Box plots show medians and interquartile ranges of detected autophagosomes; outliers (>1.53 interquartile range) are shown as black dots, n ≥ 34. Significant differences compared to wildtype are indicated with * when p value ≤ 0.05, ** when p value ≤ 0.01, *** when p value ≤ 0.001, and **** when p value ≤ 0.001. Unpaired t-test with Welch's correction. **c**, CAN1-GFP puncta colocalize with mCherry-ATG8E *in vivo*. Co-localization analyses of single plane confocal images obtained from transgenic wildtype (left panel) and *atg5* (right panel) Arabidopsis roots co-expressing mCherry-ATG8E (magenta) with CAN1-GFP (green). Seedlings were germinated 5 days prior transfer to the indicated treatment for 1 day (+/-Pi) or 5 h liquid media (+ Pi + TM; - Pi + ConA; + Pi + TM + ConA). Rectangles indicate Inset. Scale bars, 20 µm. **d**, Quantification of mCherry-ATG8E and CAN1-GFP colocalized puncta in the indicated treatments as described in a. n ≥ 5. **e-f**, loss of *CAN1* increases Arabidopsis ER stress tolerance. **e**, Top: 11 days old seedlings of wildtype, *pdr2*, *can1-c1* and *can1-c3* germinated on control or ER stress (100 ng/mL, TM) media. Bottom: Fresh weight of 5 pooled seedlings per sample, n = 17-18. **f**, Top: Germination of the indicated genotypes for eight days on Pi-sufficient (+Pi) or Pi-depleted (-Pi) conditions, scale bar = 1cm. Bottom: Primary root growth inhibition in percentage of the indicated genotypes, shown are summarized data of five independent biological experiments with each n ≥ 8. Significant differences compared to wildtype are indicated with * when p value ≤ 0.05, ** when p value ≤ 0.01, *** when p value ≤ 0.001, and **** when p value ≤ 0.001. Unpaired t-test with Welch's correction.

Figure 6

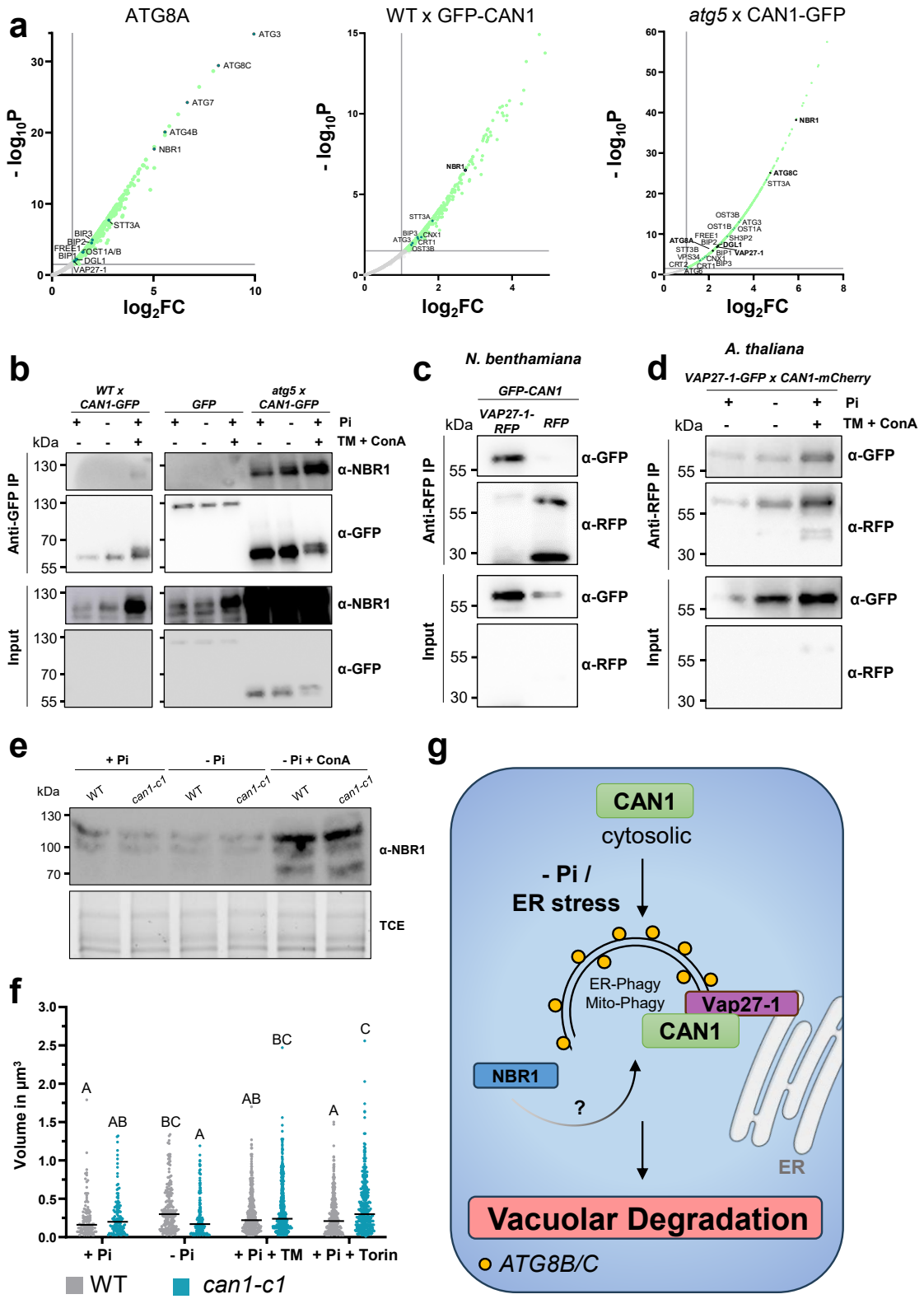

Figure 6: CAN1 interacts with NBR1 and VAP27-1 to modulate autophagosomal size. a, Enrichment of proteins interacting with ATG8A, *pUBQ10::GFP-CAN1* in wildtype and *pCAN1::CAN1-GFP* in *atg5* background in ER stress (+ TM + ConA) compared with a control expressing free GFP and represented by a volcano plot. Seedlings were germinated 10 days on liquid +Pi media prior to transfer to the indicated media. The horizontal grey line

indicates the threshold above which proteins are enriched (P value <0.03, quasi-likelihood negative binomial generalized log-linear model), and the vertical dashed line indicates the threshold where the proteins' $\log_2$FC is greater than 1. **b**, Western blot analysis from immunoprecipitation (IP) experiments using wildtype and *atg5* expressing *pCAN1::CAN1–GFP* or *pCAN1::GFP-GUS* to immunoprecipitate NBR1. Seedlings were germinated 10 days on liquid +Pi media prior to transfer to + or – Pi for 24 h or ER stress treatment with 5 µg/ml TM and 1 µM ConA for 6 h. Whole roots were harvested. The blots were probed with anti-NBR1 and anti-GFP antibodies to detect the presence of NBR1. **c-d**, CAN1 interacts with VAP27;1 in *N.benthamiana* and *A. thaliana* roots in ER stress. **c**, IP of *p35S::VAP27-1-RFP* or *p35S::mCherry-HDEL* co-expressed with *pUBQ10::GFP-CAN1* in *N.benthamiana* leaves. Input and bound proteins were visualized with anti-GFP and anti-RFP antibodies. **d**, IP of extracts of F1 Arabidopsis roots co-expressing *p35S::CAN1-mCherry* and *pVAP27-1::VAP27-1-GFP* after transfer for 24 h to Pi sufficient or deficient liquid media. ER stress was applied by incubation in +Pi with 5 µg/ml TM and 1 µM ConA containing liquid media for 6 h. Input and bound proteins were visualized by immunoblotting with anti-RFP and anti-GFP antibodies. **e**, NBR1 protein amount is not influenced by CAN1 in Pi-deprived roots. Endogenous NBR1 detection by anti-NBR1 antibody in extracts from wildtype and *can1-c1* roots germinated 5 days on +Pi media prior to transfer to +Pi, –Pi or –Pi containing 1 µM ConA liquid media for 24h. **f**, Loss of CAN1 affects autophagosome size in Pi-stressed roots. Seedlings of wildtype or *can1-c1* expressing *p35S::GFP-ATG8A* were germinated for 5 days on +Pi media prior to transfer for 24 h to +Pi or –Pi media or incubated with 5 µg/ml TM or 1µM torin for 6 h for autophagic induction. Size of GFP-ATG8A labelled puncta were measured via Arivis software and calculated volume was plotted accordingly. Scatter plot, median is shown as bold line, letters denote statistical differences at $p < 0.05$ (Two-way ANOVA and Tukey's HSD post hoc test) and $n = 20$. **g**, Model of CAN1 function in autophagy. Induction of ER stress by local root tip Pi-sensing initiates CAN1 association to the ER and interaction with VAP27-1 to enable autophagosome maturation and membrane expansion for bulky cargo engulfment (e.g. ER-fractions, organelles). Potential NBR1 recruitment of CAN1 to the mature autophagosome by an unknown signal initiates ER-detachment and vacuolar degradation.

Supplementary Figure S1

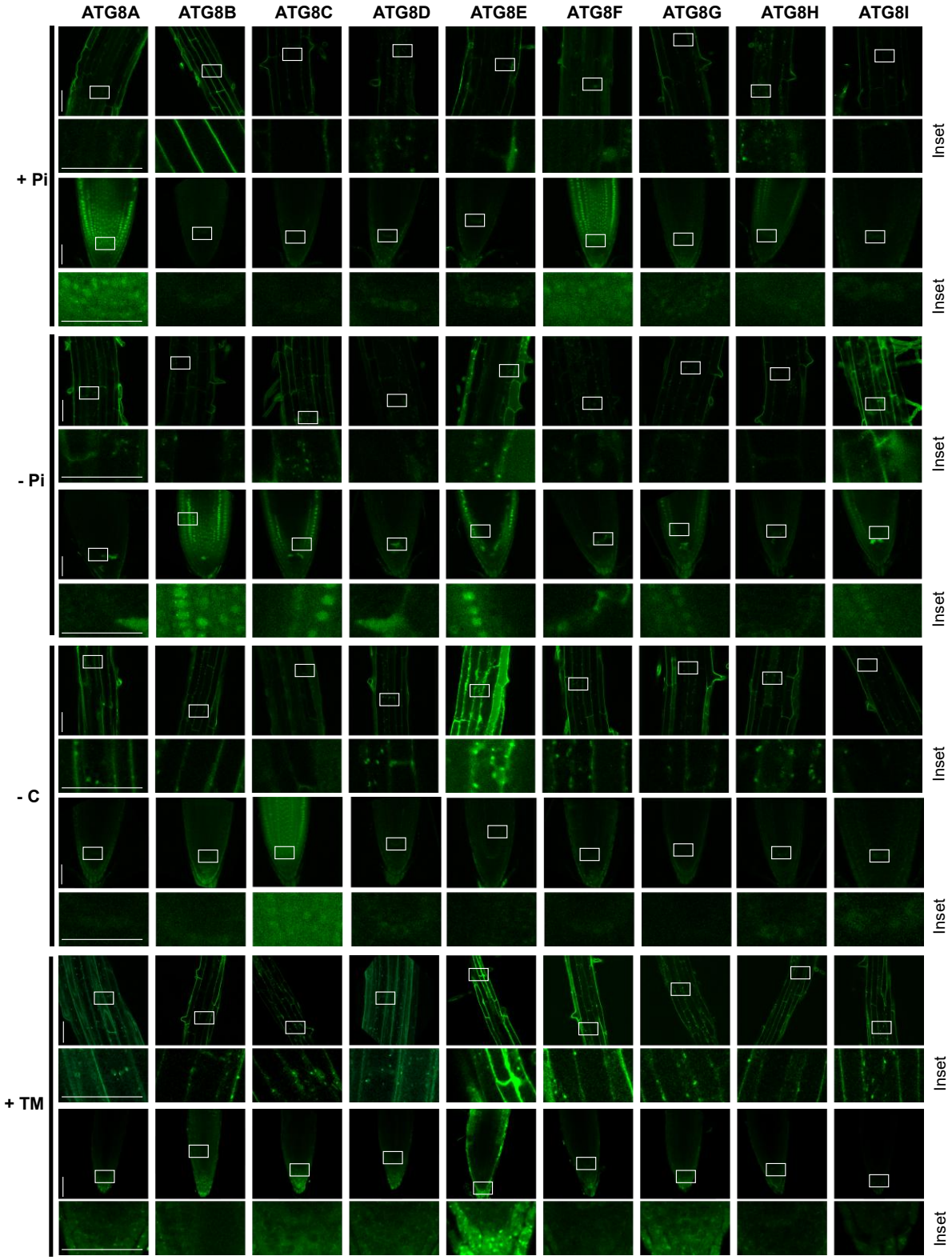

Supplementary Figure S1: Root tip ATG8 isoform specific autophagosome decoration. Seedlings were germinated 5 days prior transfer to the indicated treatment. Representative confocal microscopic images showing autophagosome formation of all 9 ATG8 isoforms (*pATG8x::GFP-ATG8x*) in the transition zone (row 1,3,5,7) or primary root tip (row 2,4,6,8) challenged with local Pi deprivation (row 3 and 4), carbon starvation (row 5 and 6) for 24 h or

5 µg/mL tunicamycin (TM) treatment (row 7 and 8) for 6-8 h, rectangle indicate Inset selection, n ≥ 10.

Supplementary Figure S2

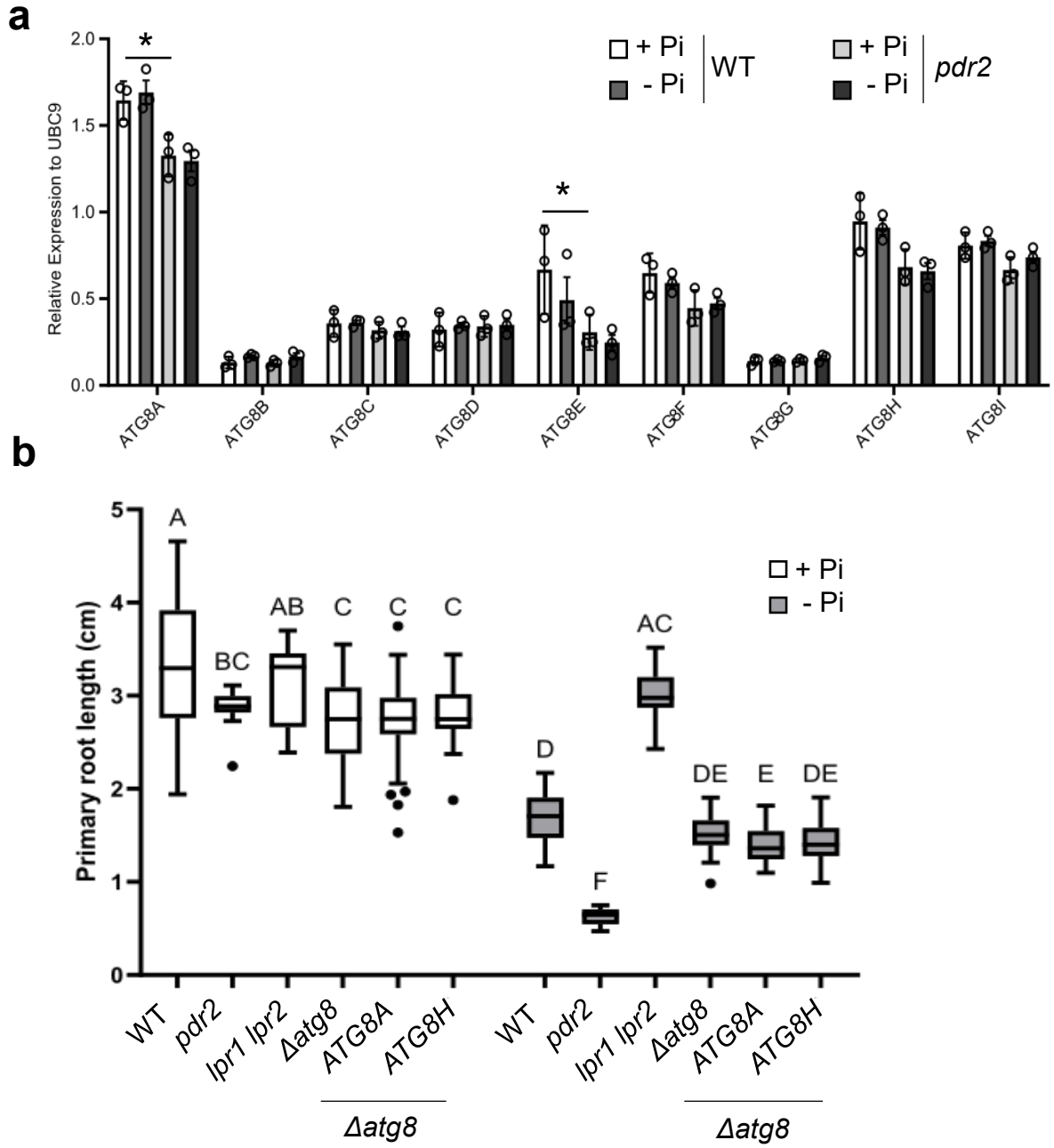

Supplementary Figure S2: Select ATG8 isoforms are involved in root tip Pi-dependent ER stress-mediated autophagy. a, Analysis of *ATG8A-I* relative transcript levels (normalized to UBC9 expression) in wildtype and *pdr2* root tips after transfer to +Pi or –Pi medium for 24 h (germinated for 5 days on +Pi) ±SD; n = 3; Two-way ANOVA, Post-hoc Tuckey, *p value ≤ 0.05. **b**, ATG8A and ATG8H fail to complement *Δatg8* sensitivity to Pi limitation. Seedlings were germinated for 5 days on +Pi media prior to transfer to medium supplemented with or without Pi (-Pi, +Pi) and imaged after 4 days. Gain of primary root extension was measured. Box plots show medians and interquartile ranges of primary root gain; outliers (>1.53 interquartile range) are shown as black dots. Letters denote statistical differences in condition at $p < 0.05$ (Two-way ANOVA and Tukey's HSD post hoc test) and $n \geq 13$-50.

Supplementary Figure S3

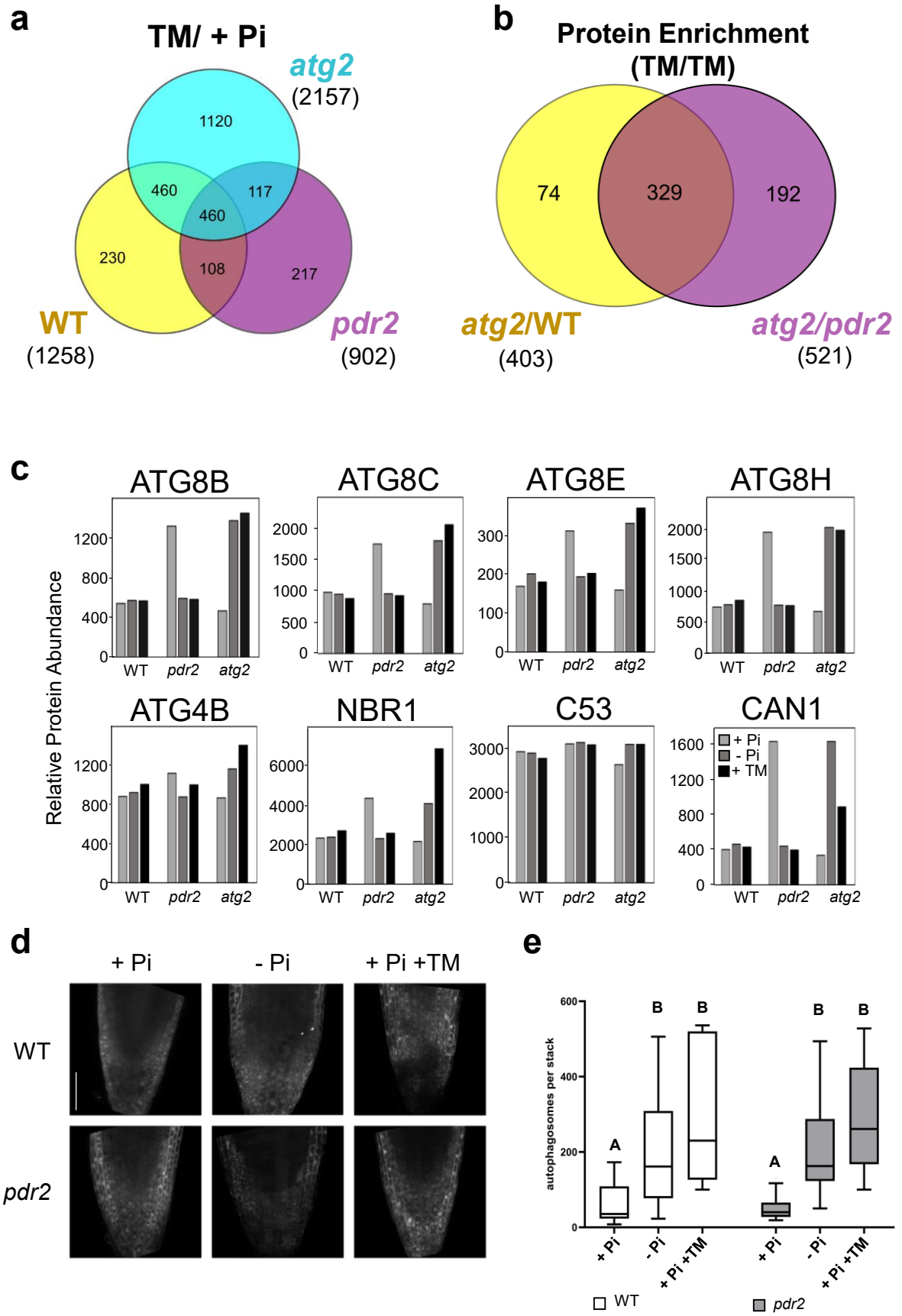

Supplementary Figure S3: ER-stress derived adaptation of root tip proteomes. a, Chemically induced ER stress impacts root proteome. Venn diagram of three overlapping pairwise comparisons for root tip TMT-MS conducted in wildtype (yellow), *pdr2* (magenta) and *atg2* (cyan) plants: wildtype (+Pi) vs wildtype (+Pi+TM) yellow cycle, *pdr2* (+Pi) vs. *pdr2* (+Pi+TM) magenta cycle, *atg2* (+Pi) vs. *atg2* (+Pi+TM) cyan cycle. Protein abundances with 0.6 > FC > 1.3. Total numbers are depicted in brackets. **b**, Overlap between proteins identified in + Pi + TM conditions enriched in *atg2* compared to wildtype (yellow) or *pdr2-1* (magenta) identified by quantitative MS, FC > 1.3. **c**, Proteins of the autophagic pathway are affected in local Pi-mediated root tip proteomic adaptation. Plotted protein abundances of ATG8B/C/E/H, ATG4B, NBR1, C53 and CAN1 in +Pi (light grey), -Pi (dark grey) and +Pi +TM (black) conditions measured via TMT-MS in wildtype, *pdr2* and *atg2.* **d,e** Autophagosome induction in Pi deprived and ER stressed root tips. **d**, GFP-ATG8A derived fluorescence in primary root tips of transgenic (*p35S::GFP-ATG8A*) wildtype and *pdr2* seedlings after germination on +Pi agar (5 d) and subsequent transfer to –Pi medium for 24 h or treatment with 5 µg/mL TM for 6 h. Shown are representative images from three independent experiments fused Z-stacks of the root tip. Scale bars, 50 µm. **e**, Quantification of GFP-ATG8 puncta in root cells per normalized area and number of slices. Box plots show medians and interquartile ranges of detected autophagosomes; outliers (>1.53 interquartile range) are shown as black dots. Letters denote statistical differences in condition at $p < 0.05$ (Two-way ANOVA and Tukey's HSD post hoc test) and $n \geq 6$.

Supplementary Figure S4

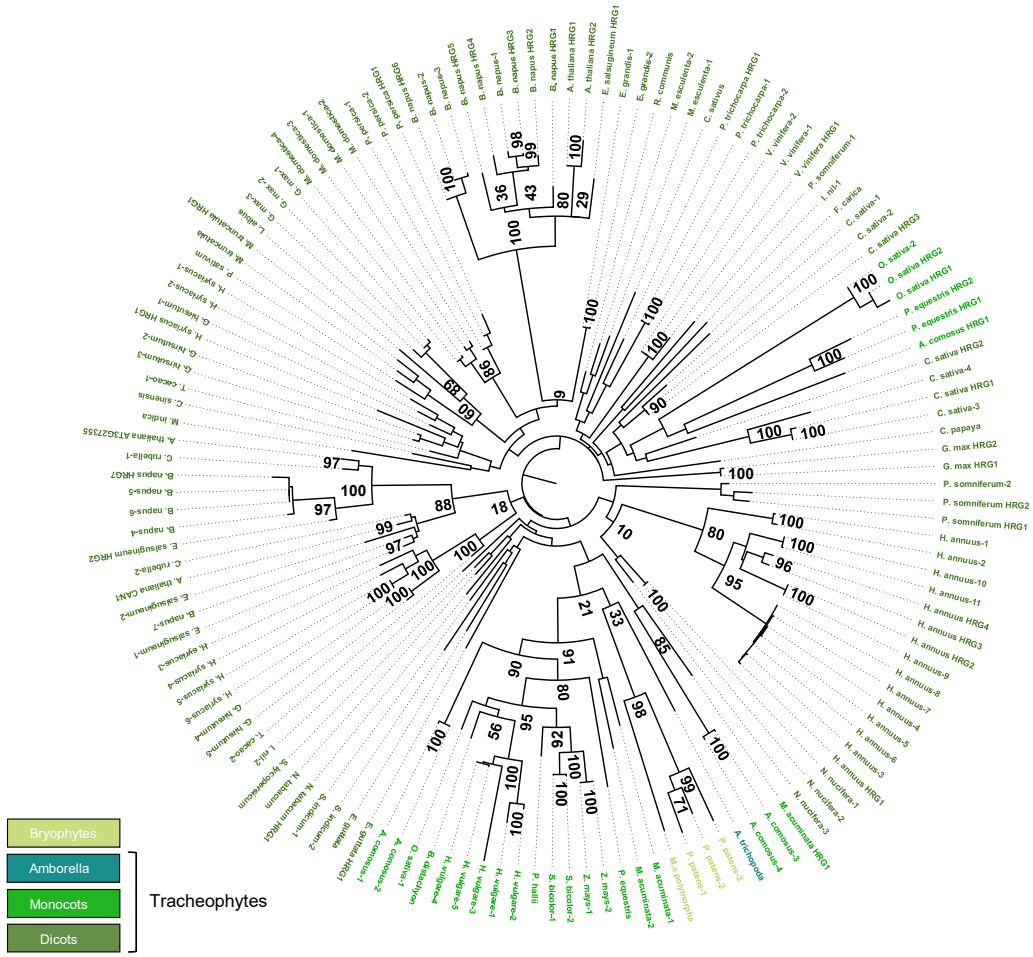

Supplementary Figure S4: CAN1 is present in most land plant species. Maximum-likelihood midpoint-rooted phylogenetic tree (250 bootstraps) of 139 predicted CAN1-like proteins (Phytozome). Identified CAN1 like proteins of bryophytes (light green), amborella (turquoise), monocots (leaf green) and dicots (dark green). Full-length CAN1-like sequences are annotated by organism in a numeric order, C-terminally truncated proteins are annotated according to *A. thaliana* HRG1 and 2 respectively.

Supplementary Figure S5

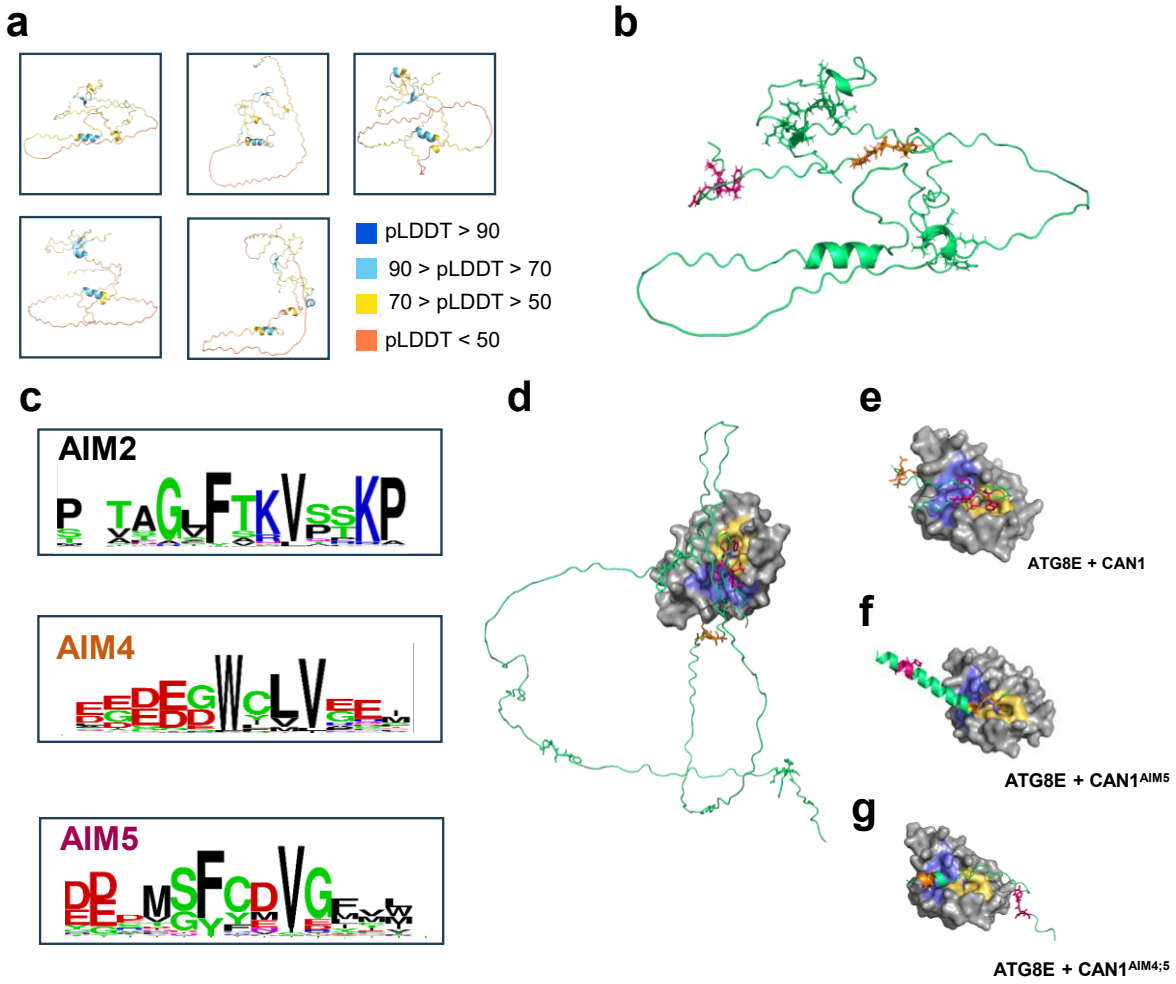

Supplementary Figure S5: CAN1 is an intrinsically disordered protein. Structure and interaction prediction of CAN1 by AlphaFold2. a, CAN1 is intrinsically disordered. Top five structure prediction by AlphaFold2 colored according to the pLDDT score of the predicted structure. **b**, CAN1 structure in green cartoon, with all five identified AIMs in stick representation (AIM1-3 green, AIM4 orange, AIM5 magenta). **c**, Specific conserved AIMs, with AIM4 and AIM5 exclusively present in full-length CAN1 proteins. **d-g** Predicted AIM-dependent interaction of full length CAN1 with ATG8E. **d**, CAN1 (cartoon, AA 192-210) interacts with ATG8E (surface representation) via AIM5 (stick, magenta), **e**, ATG8E AIM pockets, known as W-site (site 1 –yellow) and L-site (site 2 –slate blue) interacting with W202 and V205. **f**, Predicted interaction of CAN1$^{\Delta AIM5}$ (cartoon, AA 181-210) via AIM4 (stick, orange) and **g**, loss of predicted CAN1 ATG8E interaction in CAN1$^{\Delta AIM4,5}$ (cartoon, AA 181-210).

Supplementary Figure S6

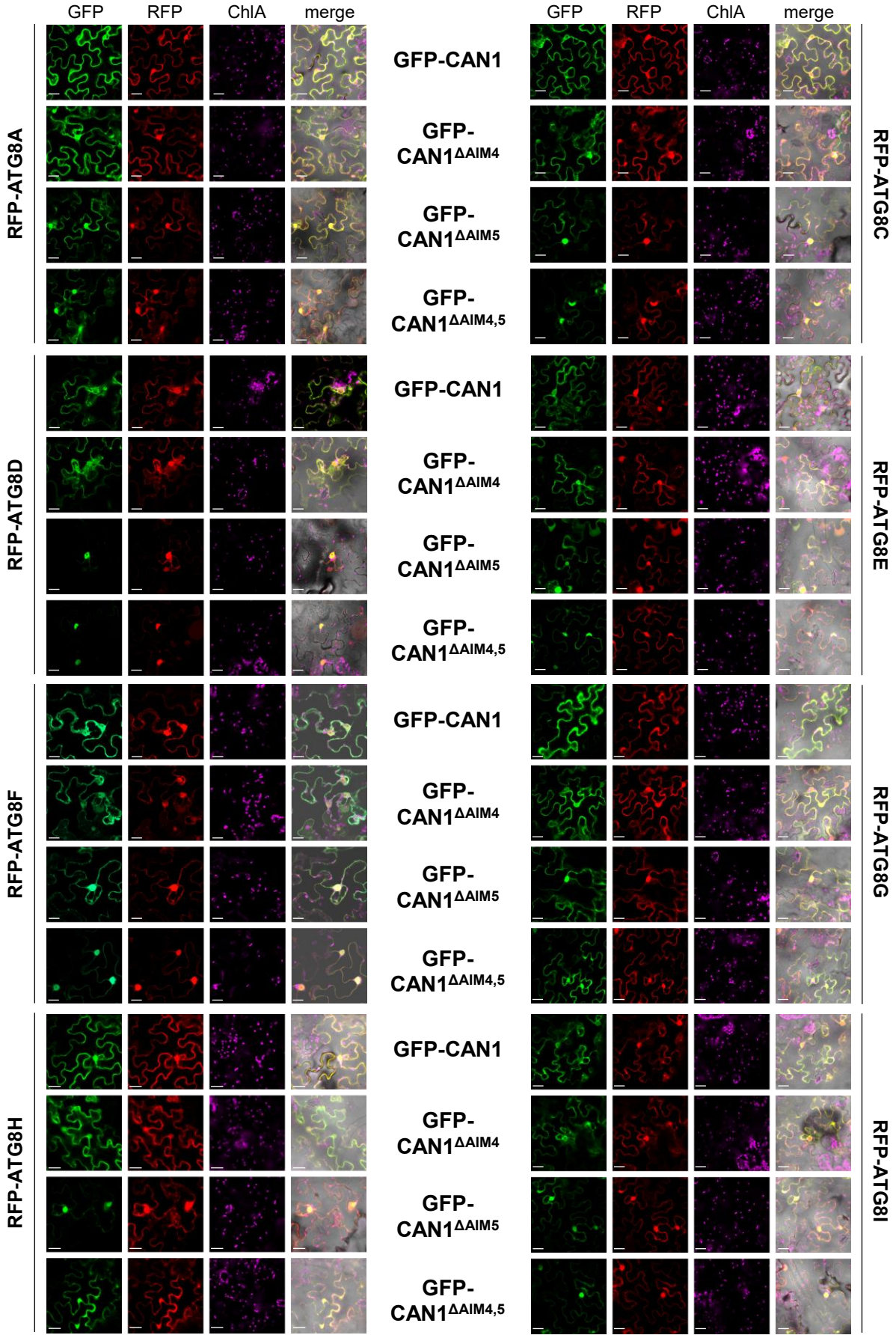

Supplementary Figure S6: CAN1 co-localizes with all ATG8 isoforms in *N. benthamiana*. Localization of GFP-CAN1 variants (CAN1, CAN1$^{\Delta AIM4}$, CAN1$^{\Delta AIM5}$ CAN1$^{\Delta AIM4/5}$) transiently co-expressed with RFP-ATG8A, C-I in *N. benthamiana*. The images are single optical sections of GFP (first column), RFP (second column), chlorophyll A (third column, blue) and merged (including bright field) signals (last column). Scale bars, 10 µm; n ≥ 3.

Supplementary Figure S7

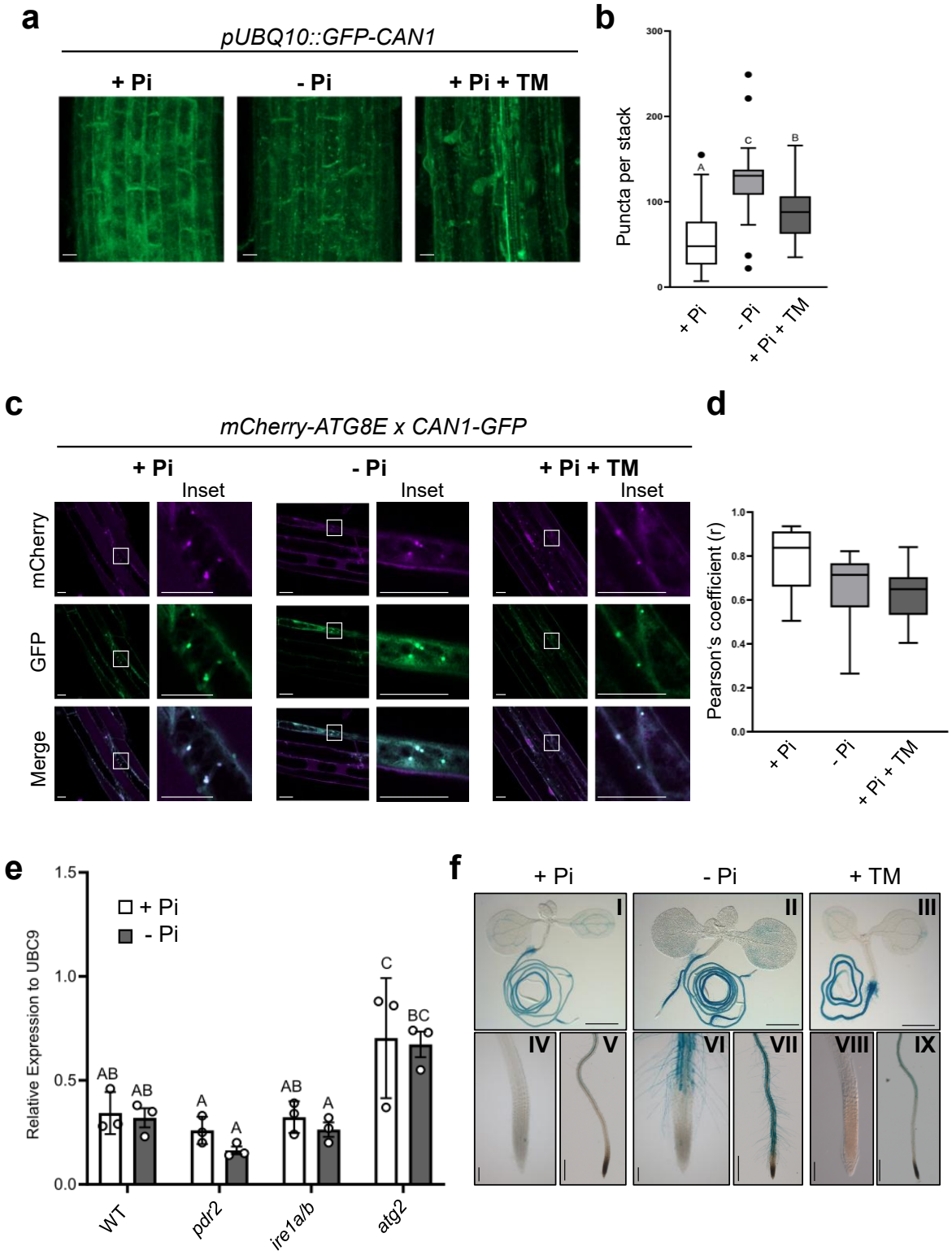

Supplementary Figure S7: CAN1 protein functions in ER stress-induced autophagy by local Pi sensing. a, GFP-CAN1 derived fluorescence in primary root tips of transgenic (*pUBQ10::GFP-CAN1*) wildtype seedlings after germination on +Pi agar (5 d) and subsequent transfer to –Pi medium for 0-24 h or treatment with 5 µg/mL TM for 6 h. Shown are representative images from three independent experiments fused Z-stacks of the transition zone. Scale bar 20 µm. **b**, Quantification of GFP-CAN1 puncta per stack in the indicated

treatments. Box plots show medians and interquartile ranges of detected puncta; outliers (>1.53 interquartile range) are shown as black dots. Letters denote statistical differences in condition at $p < 0.05$ (Two-way ANOVA and Tukey's HSD post hoc test) and $n \geq 30$. **c**, CAN1-GFP puncta colocalize with mCherry-ATG8E *in vivo*. Co-localization analyses of single plane confocal images obtained from transgenic Arabidopsis roots co-expressing mCherry-ATG8E (magenta) with CAN1-GFP (green) in wildtype. Seedlings were germinated 5 days prior transfer to the indicated treatment for 1 day (+/-Pi) or 5 h (TM). Scale bars, 20 µm, $n \geq 10$. **d**, Pearson's Coefficient (r) analysis of the colocalization of CAN1-GFP and mCherry-ATG8E. Box plots show medians and interquartile ranges with five independent measures per biological replicate, $n \geq 10$. **e**, *CAN1* expression relative to UBC9 in gain of primary root tip 1 day after transfer of wildtype, *pdr2*, *ire1a/b* and *atg2.* Letters denote statistical differences in condition at $p < 0.05$ (Two-way ANOVA and Tukey's HSD post hoc test) and $n = 3$. **f**, *pCAN1::GUS* activity in 10 days old wildtype seedlings after transfer to the indicated media for two days or incubation with TM for 6 h, $n = 3$. Overview of the seedlings (I-III) scale bar 1 cm, primary root tip (IV-IX) with IV, VI, VIII scale bar 100 µm and V, VII, IX scale bar 1mm; $n \geq 6$.

Supplementary Figure S8

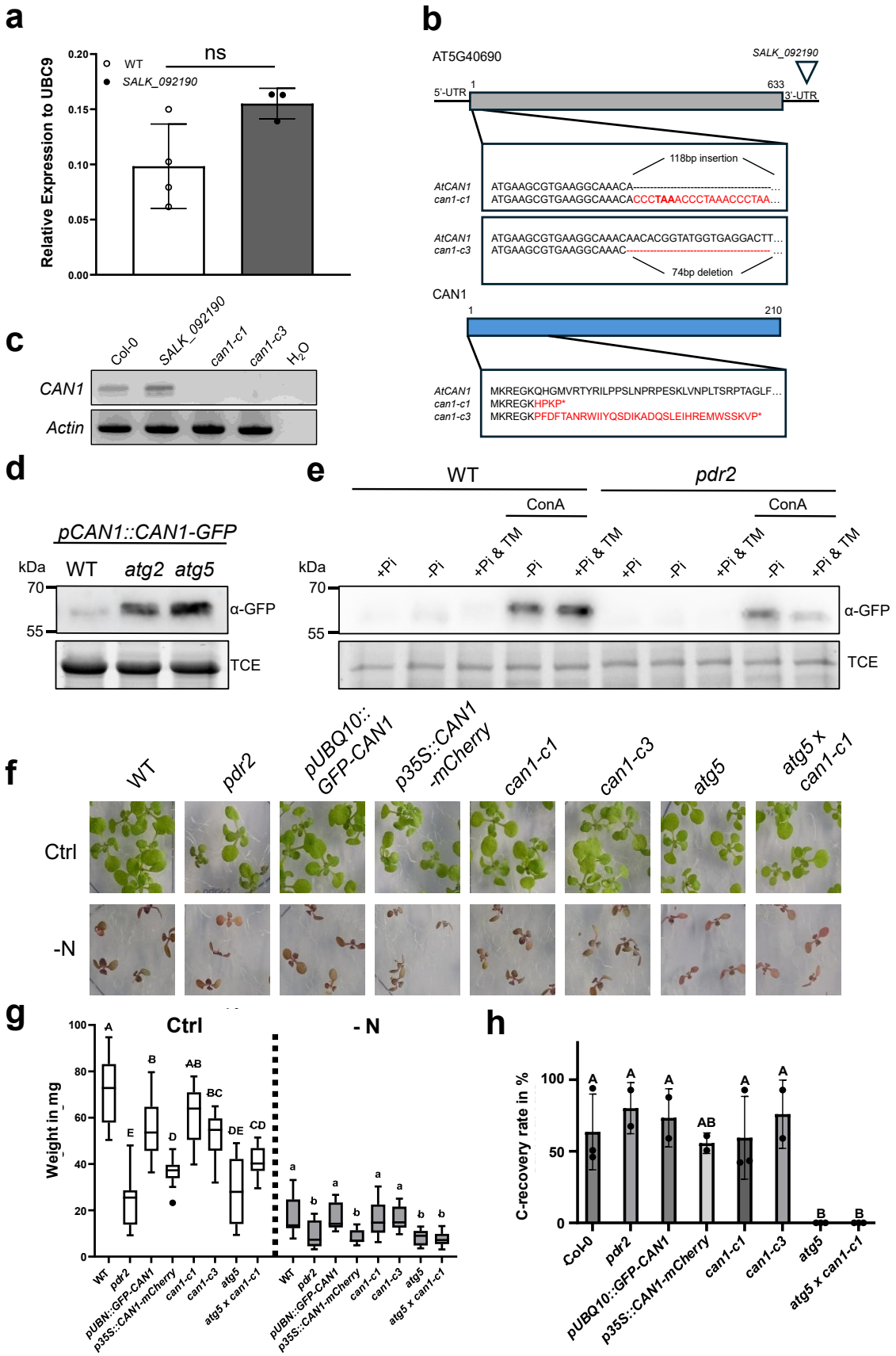

Supplementary Figure S8: CAN1 functions in ER stress-mediated autophagy. a, Transcriptional regulation of *CAN1* is not altered in SALK-Insertion line. Analysis of *CAN1* relative transcript level (normalized to UBC9 expression) of wildtype and *SALK_092190* insertion line seedlings (germinated for 5 days on +Pi media) ±SD; n ≥ 3; Students t-test. **b**, sequence analysis of *CAN1* (AT5G40690). Scheme of two *can1* CRISPR mutants, *can1-c1* and *can1-c3*. Both mutants contain deletions/insertions where *can1-c1* harbors a 118-bp insertion, while the *can1-c3* mutant possesses a 74-bp deletion. The deletions/insertions lead to amino acids changes and premature stop codons in both mutants. **c**, Expression analysis of *CAN1* by semiquantitative RT-PCR by using cDNA isolated from wildtype, *SALK_092190*, *can1-c1*, and *can1-c3* seedlings. **d**, Amount of *pCAN1::CAN1-GFP* in wildtype, *atg2* and *atg5* seedlings (germinated for 5 days on +Pi media) were analyzed by Western Blot. TCE was used as loading control, n = 4. **e**, 5-day old seedlings expressing *pCAN1::CAN1-GFP* in wildtype and *pdr2* mutant were transferred to the indicated media for 24 h, TM (300 ng/µl) ConA (1µM). Whole roots were harvested and analyzed by immunoblot. TCE was used as loading control, n = 3. **f, g** 5 days-old seedlings of the indicated genotypes were grown on full (Ctrl) and N-depleted media for 7 days. **g**, Analysis of seedling weight after treatment. Box plots show medians and interquartile ranges of primary root gain. Letters denote statistical differences in treatment condition at $p < 0.05$ (One-way ANOVA and Tukey's HSD post hoc test) and n = 8-16. **h**, Loss-of *CAN1* does not rescue carbon starvation in *atg5* mutant plants. 5 days-old seedlings of the indicated genotypes were germinated on full media, prior to carbon starvation for 12 days, followed by recovery on full media for one week, ±SD; n = 3; One-way ANOVA, Post-hoc Tuckey, *p value ≤ 0.05.

Supplementary Figure 9

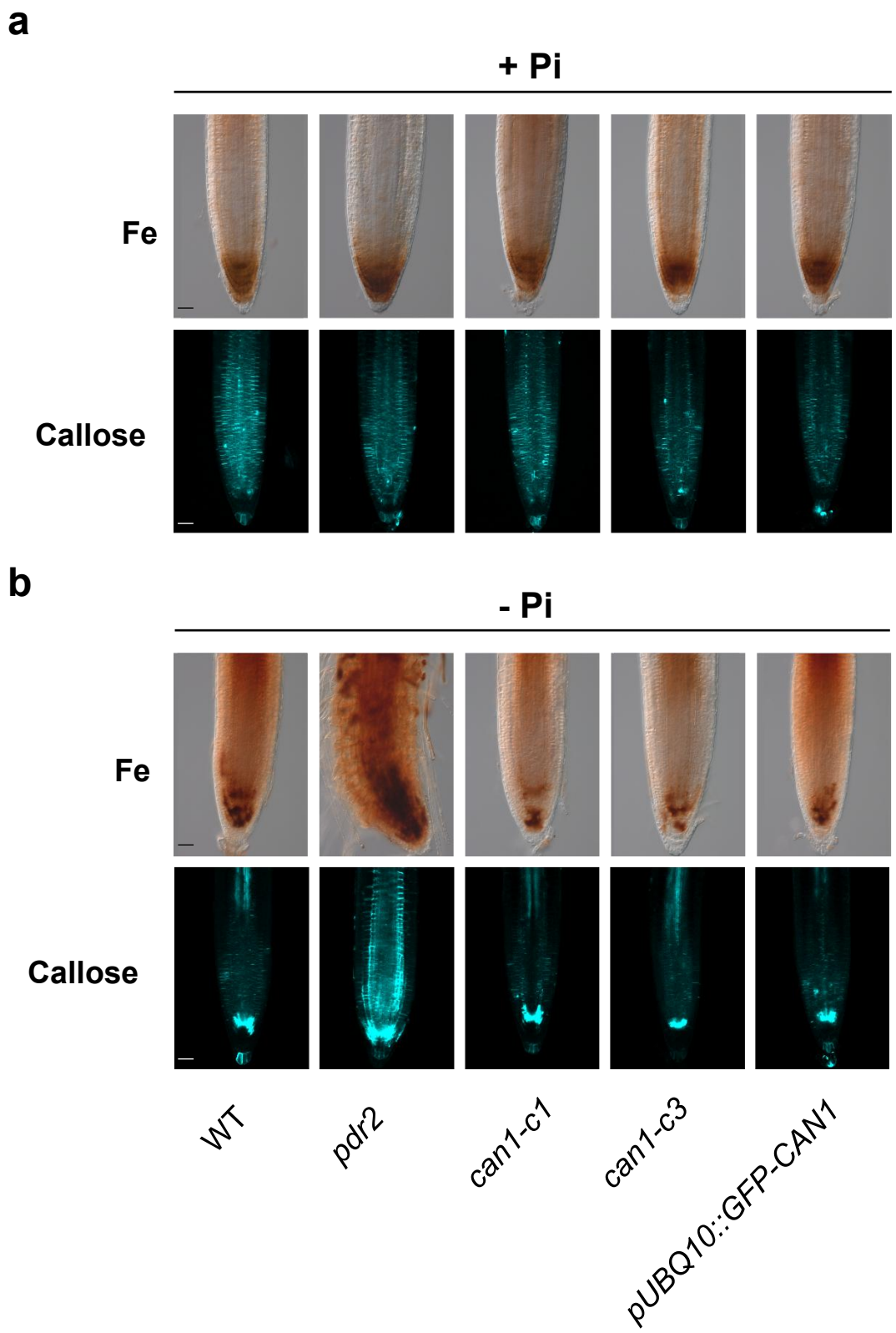

Supplementary Figure S9: LPR1-mediated local Pi response is not influenced by CAN1. a,b After germination (5 d, +Pi), seedlings were transferred to +Pi (**a**) or –Pi (**b**) medium (25 µM Fe). Top row: Three days after transfer, root tips of wildtype, *pdr2*, *can1-c1*, *can1-c3 and pUBQ10::GFP-CAN1* were monitored for Fe^{3+} accumulation by Perls staining coupled to

diaminobenzidine (DAB) intensification. Bottom row: One day after transfer, root tips were monitored for callose deposition by aniline blue staining. Shown are representative images ($n \geq 20$). Scale bars 50 µm.

Supplementary Figure S10

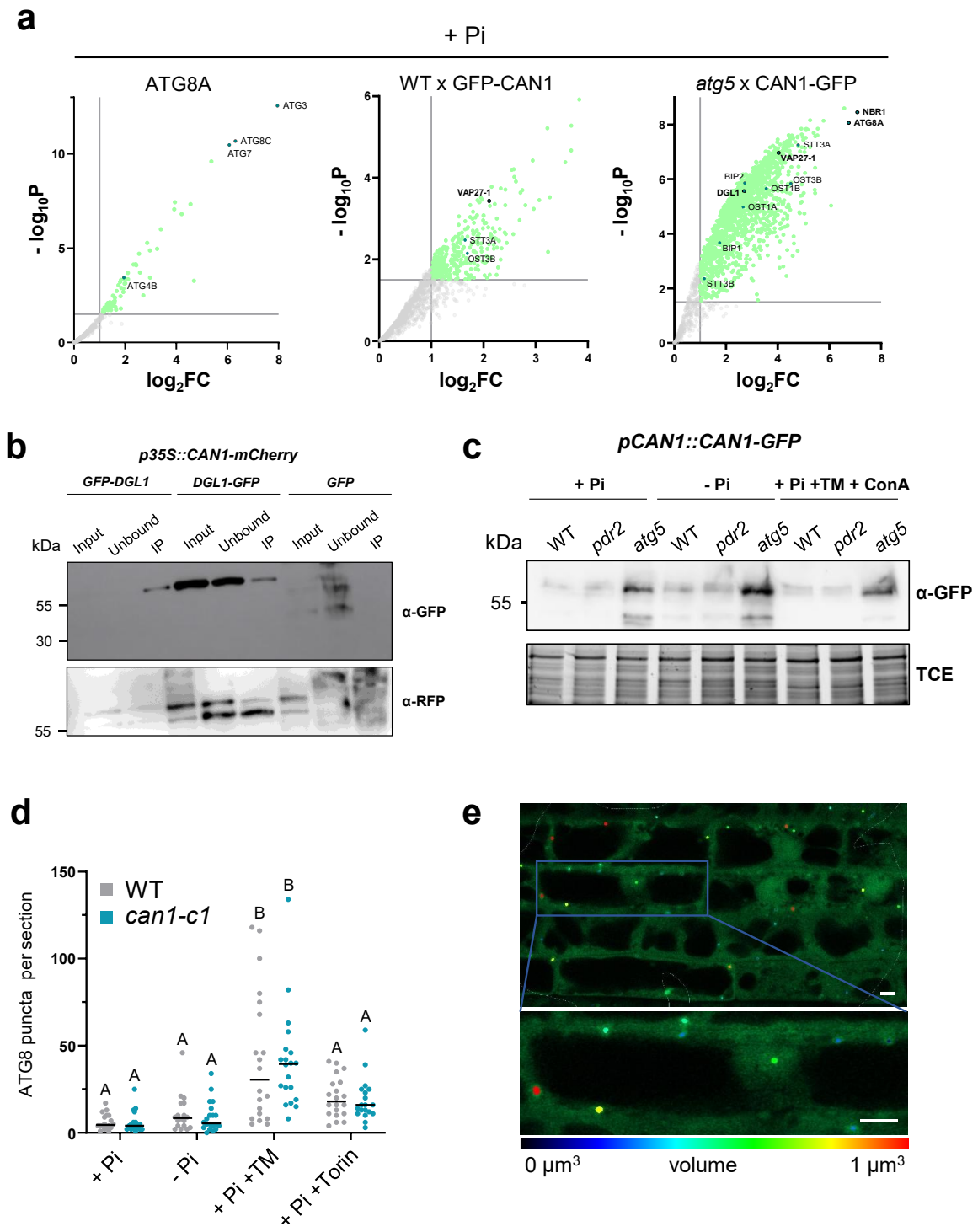

Supplementary Figure S10: CAN1 intersects with the autophagic pathway in ER stress. **a**, Enrichment of proteins interacting with *p35S::GFP-ATG8A*, *pUBQ10::GFP-CAN1* in wildtype and *pCAN1::CAN1-GFP* in *atg5* background in + Pi compared with a control expressing free GFP and represented by a volcano plot. The horizontal grey line indicates the threshold above which proteins are enriched (P value <0.03, quasi-likelihood negative binomial generalized log-linear model), and the vertical dashed line indicates the threshold where the proteins' $\log_2$FC is > 1. **b**, Western blot analysis from immunoprecipitation (IP) experiments of tobacco leaves co-infiltrated with *p35S::CAN1–mCherry* together with

p35S::DGL1-GFP, *pUBQ10::GFP-DGL1* or *p35S::GFP-HDEL.* Input and bound proteins were visualized with anti-GFP and anti-RFP antibodies, n = 3. **c**, Amount of *pCAN1::CAN1-GFP* in wildtype, *pdr2* and *atg5* roots were analyzed by immunoblot. Seedlings were germinated 5 days on +Pi prior to transfer to the indicated media for 24 h or ER stress treatment with 5 µg/ml TM and 1 µM ConA for 6 h. TCE was used as loading control, n = 4. **d**, Autophagosome quantification in roots of wildtype and *can1-c1* expressing *p35S::GFP-ATG8A.* Seedlings were germinated for 5 days on +Pi media prior to transfer for 24 h to +Pi or –Pi media or incubated with 5 µg/ml TM or 1µM torin for 6 h for autophagic induction. Scatter plot, median is shown as bold line, letters denote statistical differences at $p < 0.05$ (Two-way ANOVA and Tukey's HSD post hoc test), $n \geq 18$. **e**, Representative image of autophagosome volume quantification in Arivis. *p35S::GFP-ATG8A in* wildtype 24 h post transfer to –Pi is shown. Scale = 5 µm. Color-coded autophagosome volume according to the scale.